



**HAL**  
open science

## Chemical Differentiation and Temperature Distribution on a Few au Scale around the Protostellar Source B335

Yuki Okoda, Yoko Oya, Muneaki Imai, Nami Sakai, Yoshimasa Watanabe,  
Ana López-Sepulcre, Kazuya Saigo, Satoshi Yamamoto

► **To cite this version:**

Yuki Okoda, Yoko Oya, Muneaki Imai, Nami Sakai, Yoshimasa Watanabe, et al.. Chemical Differentiation and Temperature Distribution on a Few au Scale around the Protostellar Source B335. *The Astrophysical Journal*, 2022, 935, 10.3847/1538-4357/ac7ff4 . insu-03860313

**HAL Id: insu-03860313**

**<https://insu.hal.science/insu-03860313>**

Submitted on 18 Nov 2022

**HAL** is a multi-disciplinary open access archive for the deposit and dissemination of scientific research documents, whether they are published or not. The documents may come from teaching and research institutions in France or abroad, or from public or private research centers.

L'archive ouverte pluridisciplinaire **HAL**, est destinée au dépôt et à la diffusion de documents scientifiques de niveau recherche, publiés ou non, émanant des établissements d'enseignement et de recherche français ou étrangers, des laboratoires publics ou privés.



Distributed under a Creative Commons Attribution 4.0 International License



# Chemical Differentiation and Temperature Distribution on a Few au Scale around the Protostellar Source B335

Yuki Okoda<sup>1,2</sup> , Yoko Oya<sup>2,3</sup> , Muneaki Imai<sup>2</sup> , Nami Sakai<sup>1</sup> , Yoshimasa Watanabe<sup>4</sup> , Ana López-Sepulcre<sup>5,6</sup> , Kazuya Saigo<sup>2,7</sup> , and Satoshi Yamamoto<sup>2,3</sup>

<sup>1</sup>RIKEN Cluster for Pioneering Research, 2-1, Hirosawa, Wako-shi, Saitama 351-0198, Japan; [yuki.okoda@riken.jp](mailto:yuki.okoda@riken.jp)

<sup>2</sup>Department of Physics, The University of Tokyo, 7-3-1, Hongo, Bunkyo-ku, Tokyo 113-0033, Japan

<sup>3</sup>Research Center for the Early Universe, The University of Tokyo, 7-3-1, Hongo, Bunkyo-ku, Tokyo 113-0033, Japan

<sup>4</sup>Materials Science and Engineering, College of Engineering, Shibaura Institute of Technology, 3-7-5 Toyosu, Koto-ku, Tokyo 135-8548, Japan

<sup>5</sup>Univ. Grenoble Alpes, CNRS, IPAG, F-38000 Grenoble, France

<sup>6</sup>Institut de Radioastronomie Millimétrique, F-38406 Saint-Martin d'Hères, France

<sup>7</sup>Graduate School of Science and Engineering, Kagoshima University, 1-21-40 Korimoto Kagoshima-city Kagoshima, 890-0065, Japan

Received 2022 May 9; revised 2022 July 1; accepted 2022 July 8; published 2022 August 23

## Abstract

Resolving physical and chemical structures in the vicinity of a protostar is of fundamental importance for elucidating their evolution to a planetary system. In this context, we have conducted 1.2 mm observations toward the low-mass protostellar source B335 at a resolution of  $0''.03$  with the Atacama Large Millimeter/submillimeter Array. More than 20 molecular species including HCOOH, NH<sub>2</sub>CHO, HNCO, CH<sub>3</sub>OH, CH<sub>2</sub>DOH, CHD<sub>2</sub>OH, and CH<sub>3</sub>OD are detected within a few tens au around the continuum peak. We find a systematic chemical differentiation between oxygen-bearing and nitrogen-bearing organic molecules by using the principal component analysis for the image cube data. The distributions of the nitrogen-bearing molecules are more compact than those of the oxygen-bearing ones except for HCOOH. The temperature distribution of the disk/envelope system is revealed by a multiline analysis for each of HCOOH, NH<sub>2</sub>CHO, CH<sub>3</sub>OH, and CH<sub>2</sub>DOH. The rotation temperatures of CH<sub>3</sub>OH and CH<sub>2</sub>DOH at the radius of  $0''.06$  along the envelope direction are derived to be 150–165 K. On the other hand, those of HCOOH and NH<sub>2</sub>CHO, which have a smaller distribution, are 75–112 K, and are significantly lower than those for CH<sub>3</sub>OH and CH<sub>2</sub>DOH. This means that the outer envelope traced by CH<sub>3</sub>OH and CH<sub>2</sub>DOH is heated by additional mechanisms rather than protostellar heating. We here propose the accretion shock as the heating mechanism. The chemical differentiation and the temperature structure on a scale of a few au provide us with key information to further understand chemical processes in protostellar sources.

*Unified Astronomy Thesaurus concepts:* [Star formation \(1569\)](#); [Young stellar objects \(1834\)](#); [Interstellar molecules \(849\)](#); [Protostars \(1302\)](#)

## 1. Introduction

Complex organic molecules (COMs), consisting of more than six atoms with one carbon atom at least, are important species for understanding the molecular evolution in the universe. They have extensively been found in various environments of low-mass star formation: quiescent dense clouds, pre-stellar cores (e.g., Bacmann et al. 2012; Cernicharo et al. 2012; Ceccarelli et al. 2017; Soma et al. 2018; Scibelli & Shirley 2020; Jiménez-Serra et al. 2021; Scibelli et al. 2021), disk/envelope systems of protostellar cores (e.g., Cazaux et al. 2003; Bottinelli et al. 2004; Kuan et al. 2004; Pineda et al. 2012; Jørgensen et al. 2016; Oya et al. 2016, 2018; Lee et al. 2019; Imai et al. 2019; Bianchi et al. 2020; Manigand et al. 2020; van Gelder et al. 2020; Martín-Doménech et al. 2021; Nazari et al. 2021; Tychoniec et al. 2021; Chahine et al. 2022), and outflow shock regions around protostars (e.g., Arce et al. 2008; Sugimura et al. 2011; Codella et al. 2020; De Simone et al. 2020). A chemical differentiation between nitrogen-bearing and oxygen-bearing species has long been recognized in high-mass protostellar clusters (e.g., Blake et al. 1987; Beuther et al. 2005; Fontani et al. 2007; Crockett et al. 2015; Feng et al. 2015; Wright et al. 1996; Wyrowski et al. 1999)

and a low-mass binary source (Kuan et al. 2004; Caux et al. 2011; Calcutt et al. 2018). In recent years, Atacama Large Millimeter/submillimeter Array (ALMA) observations reveal the small-scale chemical differentiation in each single protostellar source (Oya et al. 2017; Csengeri et al. 2019; Okoda et al. 2021; Nazari et al. 2021), where the nitrogen-bearing ones tend to have a more compact distribution than oxygen-bearing ones. Further differentiation among oxygen-bearing molecules has been reported. For instance, HCOOH shows a similar trend to the nitrogen-bearing COMs in low-mass and high-mass protostellar sources, although it is classified as an oxygen-bearing molecule (e.g., Oya et al. 2017; Csengeri et al. 2019). The observational results indicate increasing complexity of chemical structures on a small scale around a protostar in interstellar clouds and star-forming regions.

Although the chemical processes responsible for chemical differentiation have been investigated in the laboratory (e.g., Ioppolo et al. 2011) and theoretical works (e.g., Charnley et al. 1992; Caselli et al. 1993; Garrod et al. 2008; Vasyunin et al. 2017; Aikawa et al. 2020; Garrod et al. 2022), our understanding is far from complete. According to the chemical network calculations by Aikawa et al. (2020), oxygen-bearing COMs and nitrogen-bearing COMs appear in almost the same region around the protostar. Thus, the observed chemical differentiation is not well explained theoretically, and the chemical pathways/formation mechanisms responsible for the differentiation are still an open question. To step forward, the temperature structure around the



Original content from this work may be used under the terms of the [Creative Commons Attribution 4.0 licence](#). Any further distribution of this work must maintain attribution to the author(s) and the title of the work, journal citation and DOI.

protostar needs to be clarified in detail, because it is tightly related to the chemical structure (e.g., Jørgensen et al. 2018; Taquet et al. 2019; Oya & Yamamoto 2020; van Gelder et al. 2020; van't Hoff et al. 2020a, 2020b; Ambrose et al. 2021). Hence, we here investigate the molecular distributions and temperature structure around the low-mass protostellar source B335, which is rich in COMs.

B335 is a Bok globule (Keene et al. 1980) harboring the Class 0 protostellar source, IRAS 19347+0727. As this source is in an isolated condition without influences of nearby star formation activities, it has been used as an excellent test bed for star formation studies (e.g., Hirano et al. 1988; Evans et al. 2015; Yen et al. 2015; Imai et al. 2016, 2019; Bjerkeli et al. 2019). The distance to B335 was reported to be 90–120 pc, which was evaluated from stellar spectral energy distributions of nearby stars (Olofsson & Olofsson 2009). Therefore, 100 pc was often employed as the conventional distance to B335 in previous works (e.g., Bjerkeli et al. 2019; Imai et al. 2016, 2019). Recently, Watson (2020) reported the distance to HD184982, which is thought to be associated with B335, to be 164.5 pc, by using the Gaia Data Release (DR) 2 parallax data, and hence, we employ the 165 pc distance in this study. Hereafter, we represent the physical values corrected for the distance of 165 pc, when we refer to the previous results. The bolometric temperature ( $T_{\text{bol}}$ ) and the bolometric luminosity ( $L_{\text{bol}}$ ) are 37 K (Andre et al. 2000) and  $1.6 L_{\odot}$  (Kang et al. 2021), respectively. A bipolar outflow extending along the east-to-west direction (P.A.  $\sim 90^{\circ}$ ) has been detected with single-dish and interferometric observations (e.g., Hirano et al. 1988, 1992; Stutz et al. 2008; Bjerkeli et al. 2019). It is almost parallel to the plane of the sky, where the inclination angle is reported to be between  $3^{\circ}$  and  $10^{\circ}$  (Hirano et al. 1988; Stutz et al. 2008).

Some observational works on the disk/envelope system of this source have been carried out with ALMA. Evans et al. (2015) and Yen et al. (2015) indicate that the infall motion dominates on a 100 au scale around the protostar without a clear rotation motion at a spatial resolution of  $0''.3$ . Yen et al. (2015) estimate the protostellar mass to be  $0.08 M_{\odot}$  from the marginal rotation feature seen in the  $\text{C}^{18}\text{O}$  data by assuming the infalling–rotating motion. Later, higher-angular-resolution observations have revealed a clear rotation structure along the disk/envelope system (P.A.  $\sim 0^{\circ}$ ) at a  $\sim 15$  au scale (Imai et al. 2019). The methanol ( $\text{CH}_3\text{OH}$ ) and formic acid ( $\text{HCOOH}$ ) lines are seen in the vicinity of the protostar, which reveal the velocity gradient along the envelope direction. Imai et al. (2019) apply the infalling–rotating envelope (IRE) model (Oya et al. 2014) to these velocity structures and derive the protostellar mass and the radius of the centrifugal barrier to be  $0.03$ – $0.1 M_{\odot}$  and  $<8$  au, respectively. Bjerkeli et al. (2019) independently report the velocity gradient in the  $\text{CH}_3\text{OH}$  and  $\text{SO}_2$  lines and find that it is consistent with a pure free fall or a Keplerian rotation with the protostellar mass of  $0.08 M_{\odot}$ . They also estimate the dust mass from the dust continuum emission within 12 au to be  $8 \times 10^{-4} M_{\odot}$ , which is comparable to the mass  $2.0 \times 10^{-3} M_{\odot}$  derived for the area within the radius of 41 au by Evans et al. (2015). Note that the referred masses are corrected for the 165 pc distance.

As well as the above physical structures, B335 has interesting features from the chemical point of view. The CO, CN,  $\text{HCO}^+$ , HCN, HNC,  $\text{N}_2\text{H}^+$ ,  $\text{H}_2\text{CO}$ , CS, CCH, and  $c\text{-C}_3\text{H}_2$  lines were detected on a few hundreds to thousands au scale with ALMA (Evans et al. 2015; Imai et al. 2016). Distributions of the CCH and  $c\text{-C}_3\text{H}_2$  emission around the protostar indicate the warm carbon-

chain chemistry (WCCC) nature of this source (Sakai et al. 2008; Sakai & Yamamoto 2013). For the inner region at a few tens au scale, various COM lines, such as acetaldehyde ( $\text{CH}_3\text{CHO}$ ), methyl formate ( $\text{HCOOCH}_3$ ), and formamide ( $\text{NH}_2\text{CHO}$ ), were detected with ALMA by Imai et al. (2016). This feature is the characteristic of a hot corino (Cazaux et al. 2003; Herbst & van Dishoeck 2009). Hence, B335 is recognized as the WCCC source containing a hot corino: namely, a hybrid source like L483 (Oya et al. 2017) and CB68 (Imai et al. 2022). As the chemical structure of hybrid sources is consistent with the chemical model (Aikawa et al. 2008, 2020), they are thought to be a common occurrence. However, their identification requires high-sensitivity and high-resolution observations, which makes for a small number of the identified sources. Note that we now know more than 20 hot corino sources and a few WCCC sources, some of which may be hybrid sources.

Nevertheless, the hot corino of B335 is so tiny (within a few 10 au) that it has not well been resolved spatially. This situation prevents us from detailed discussions of the chemical processes occurring there. To further elucidate the physical and chemical structures of the disk/envelope system within a few tens au scale and their mutual relation, we have observed COMs at the angular resolution ( $0''.03 \times 0''.02$ ) with ALMA. We explore chemical differentiation among COMs in the hot corino by using the principal-component analysis for the cube data (PCA-3D) in Section 3. We also derive the temperature structure within a hot corino from the multiline analyses of  $\text{HCOOH}$ ,  $\text{NH}_2\text{CHO}$ ,  $\text{CH}_2\text{DOH}$ , and  $\text{CH}_3\text{OH}$  (Section 4) and discuss it in relation to the chemical differentiation (Section 5).

## 2. Observation

Four blocks of the single-point ALMA observations toward B335 were carried out with the Band 6 receiver in the Cycle 6 operation on 2019 June 10, 12, 13, and 23. The observation parameters are summarized in Table 1. We combined these visibility data in the  $uv$  plane. The field center was taken to be  $(\alpha_{2000}, \delta_{2000}) = (19^{\text{h}}37^{\text{m}}00^{\text{s}}.898, +07^{\circ}34'09''.528)$ . In all the observations, 52 antennas were used, where the baseline length ranged from 83 to 16,196 m. The total on-source time was 180.2 minutes. The primary beam (half-power beam) width was  $23''.7$ . The largest angular size is  $0''.3$  for all these observations. The bandpass calibrator, the flux calibrator, and the pointing calibrator were J1924-2914. The phase calibrator was J1938+0448.

The data were reduced using the Common Astronomy Software Applications (CASA) package 5.8.0 (McMullin et al. 2007) as well as a modified version of the ALMA calibration pipeline. Phase self-calibration was performed by using the continuum data, and then the solutions were applied to the spectral line data. After the self-calibration procedures, the data images were prepared by using the CLEAN algorithm, where the Briggs' weighting with a robustness parameter of 0.5 was employed. The original synthesized beam size is typically  $0''.03 \times 0''.02$  (P.A.  $-30^{\circ}$ ).

## 3. Small-scale Chemical Differentiation

### 3.1. Dust Continuum

Figures 1(a) and (b) show the dust continuum emission at 1.2 mm observed in this study. It is single-peaked with a slight elongation along the north–south direction, which is consistent with the disk/envelope direction (P.A.  $\sim 0^{\circ}$ ). This feature is similar to the continuum emission reported previously

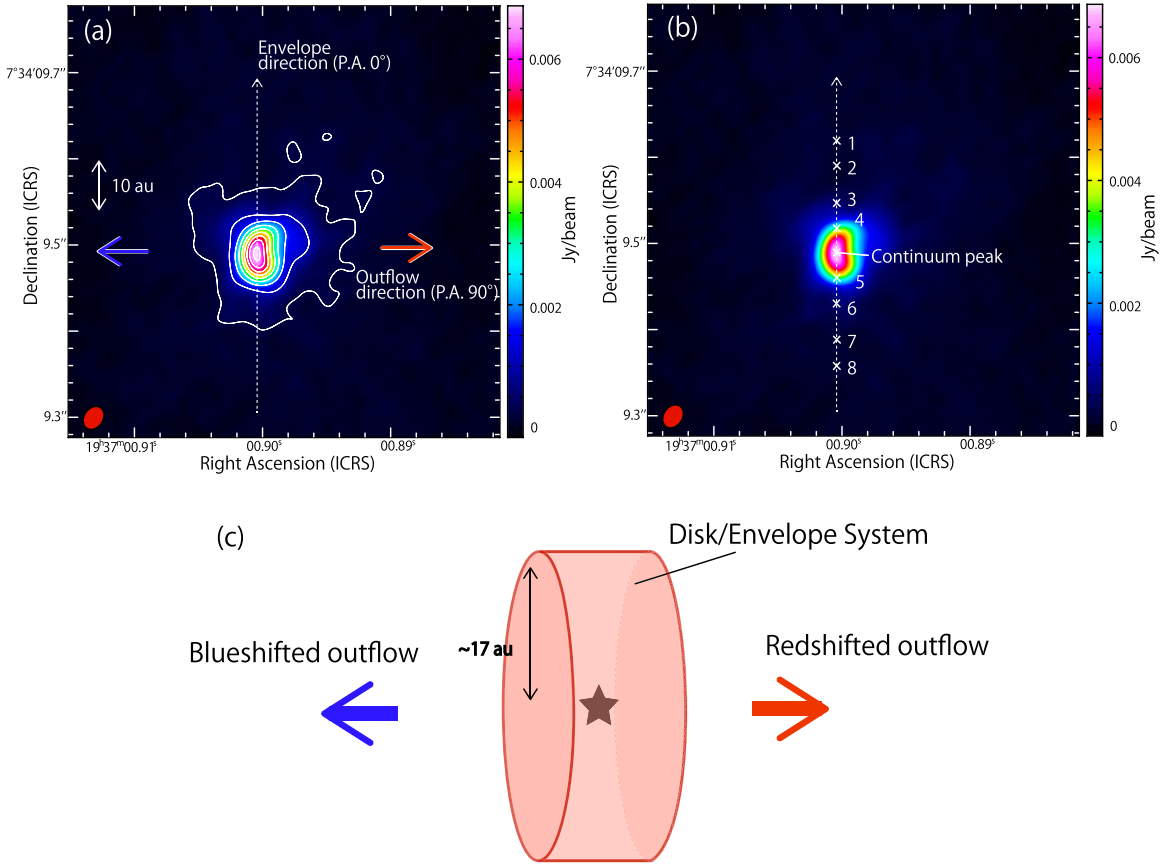


**Figure 1.** (a, b) Dust continuum emission at 1.2 mm. (a) Contour levels are every  $10\sigma$  from  $3\sigma$ , where  $\sigma$  is  $0.08 \text{ mJy beam}^{-1}$ . The horizontal and vertical dashed arrows show the outflow and envelope directions, respectively. (b) The cross marks in the right panel correspond to the positions for the derivation of the rotation temperature and the column density (Section 4.2; Table 5). The numbers indicate the positions presented in Table 5. (c) Schematic illustration of the disk/envelope system and outflow configuration in B335.

**Table 1**  
Observation Parameters<sup>a</sup>

Execution block	1 <sup>b</sup>	2 <sup>c</sup>	3 <sup>d</sup>	4 <sup>e</sup>
Observation date	2019 Jun 10	2019 Jun 12	2019 Jun 13	2019 Jun 23
Time on source (minutes)	45.05	44.93	45.12	45.10
Number of antennas	49	44	47	48
Observation frequency (GHz)	244.8–264.0			
Primary beamwidth (")	23.7			
Total bandwidth (GHz)	0.234			
Continuum bandwidth (GHz)	0.234			
Baseline range (m)	83–16196			
Bandpass calibrator	J1924-2914			
Phase calibrator	J1938+0448			
Flux calibrator	J1924-2914			
Pointing calibrator	J1924-2914			
$\sigma$ ( $\text{mJy beam}^{-1}$ $\text{channel}^{-1}$ )	1.0			

#### Notes.

<sup>a</sup> These observations are conducted with the Band 6 receiver of ALMA.

<sup>b</sup> [uid://A002/Xdd7b18/X2f30](https://doi.org/10.26434/chemrxiv-2022-08-01)

<sup>c</sup> [uid://A002/Xdd7b18/Xa010](https://doi.org/10.26434/chemrxiv-2022-08-01)

<sup>d</sup> [uid://A002/Xdd7b18/X66c](https://doi.org/10.26434/chemrxiv-2022-08-01)

<sup>e</sup> [uid://A002/Xdd7b18/X73f4](https://doi.org/10.26434/chemrxiv-2022-08-01)

(Imai et al. 2016; Bjerkeli et al. 2019). Further, the dust emission in this work shows a faint extension to the northwest. Its peak position and peak intensity are derived from a 2D Gaussian fit to the image to be  $(\alpha_{2000}, \delta_{2000}) = (19^{\text{h}}37^{\text{m}}00^{\text{s}}90, +7^{\circ}34'09''.49)$  and  $6.142 \pm 0.047 \text{ mJy beam}^{-1}$ , respectively. The major and minor axes are  $0''.055 \pm 0''.061$  and  $0''.043 \pm 0''.050$ , respectively (P.A.  $177^{\circ} \pm 2^{\circ}$ ). The intensity is consistent with the previous report ( $4.8 \text{ mJy beam}^{-1}$  at 230 GHz with the  $0''.03$  beam; Bjerkeli et al. 2019), if the slight difference of the observing frequency is considered. As shown in the schematic picture of Figure 1(c), the disk/envelope system of this source is close to edge-on with respect to the line of sight (Hirano et al. 1988; Stutz et al. 2008).

### 3.2. Principal-component Analysis for the Cube Data (PCA-3D)

As reported by Imai et al. (2019), COMs are rich in B335 and are concentrated in a vicinity of the protostar. In our higher-resolution ( $0''.03$ ) observations, more than 30 lines of COMs have also been observed, as shown in the observed spectrum toward the continuum peak position (Figure 2). To the best of our knowledge, this is the first study of COMs other than  $\text{CH}_3\text{OH}$  around a low-mass protostar at the high resolution of a few au, where the  $\text{CH}_3\text{OH}$  line was observed at a similar resolution (Bjerkeli et al. 2019). The detected lines include oxygen-bearing molecules (e.g.,  $\text{CH}_3\text{OH}$ ,  $\text{CH}_3\text{OCHO}$ ,  $\text{CH}_3\text{CHO}$ ,  $\text{HCOOH}$ ), nitrogen-bearing

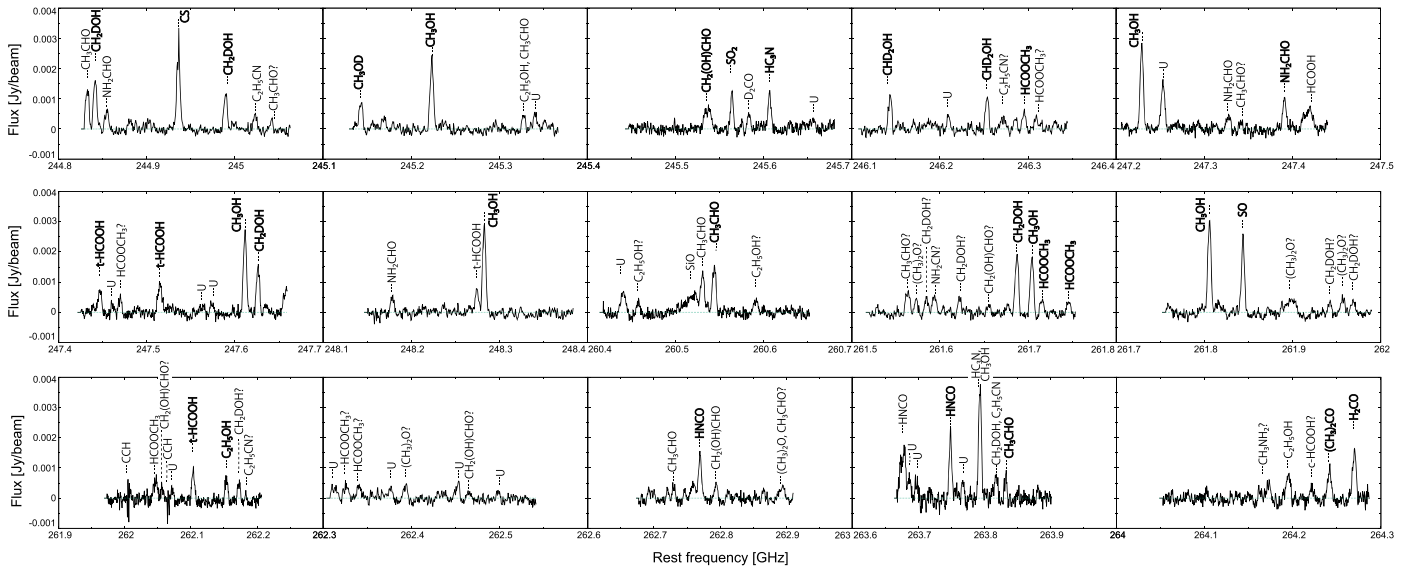


**Figure 2.** Overview of the observed spectra for a circular region with a diameter of  $0''.3$  centered at the continuum peak position. The lines that have not been clearly identified are represented by a question mark. “U” means an unidentified line. The lines used in the PCA are boldfaced.

molecules (HNC,  $\text{NH}_2\text{CHO}$ ,  $\text{HC}_3\text{N}$ ), and deuterated species of  $\text{CH}_3\text{OH}$  ( $\text{CH}_2\text{DOH}$ ,  $\text{CHD}_2\text{OH}$ , and  $\text{CH}_3\text{OD}$ ). Here, the line identification is based on the spectral line databases, the CDMS (Endres et al. 2016) and JPL catalog (Pickett et al. 1998), except for  $\text{CHD}_2\text{OH}$  (Mukhopadhyay 2016) and  $\text{CH}_3\text{OD}$  (Duan et al. 2003).

Principal-component analysis (PCA) is a kind of multivariate analyses to find orthogonal principal coordinates representing the data and is often used to reduce the dimensions of the data by transforming the original coordinates into a smaller set of orthogonal coordinates containing most of the information (Jolliffe 1986). It is a useful method to understand molecular distributions systematically, as reported previously (e.g., Spezzano et al. 2017; Nagy et al. 2019; Okoda et al. 2020, 2021). In practice, we look for the orthogonal coordinates by diagonalizing the correlation matrix or the covariance matrix of the data. The coordinates thus found are called “principal components (PCs)”, and the main features of the original data can be represented by a few PCs. In particular, Okoda et al. (2021) successfully perform a PCA for the molecular distributions including the velocity structures (PCA for the cube data: PCA-3D) in L483.

In this paper, we conduct PCA-3D of B335 to systematically reveal the small-scale chemical differentiation among these molecules in the disk/envelope system. We select 32 lines for the PCA, as listed in Table 2, and they are boldfaced in Figure 2. Here, well-isolated lines without contamination are used. The molecular lines blended with other lines are excluded (e.g., SiO and  $\text{CH}_3\text{CHO}$  around 260 GHz). Moreover, the molecular lines that are too weak to give enough data points above 3 times the rms noise level in the cube data (Table 2) are excluded, because the correlation coefficients with the distributions of other lines are not well derived. In Table 2, the molecular lines are listed in a decreasing order of the first principal component (PC1) derived later in the PCA-3D for easy comparison with the PCA results. Figure 3 shows the integrated intensity (moment 0) maps of these lines. Although all molecular lines show a round distribution around the protostar, some features are seen. A compact intensity depression toward the protostar is probably due to the high

dust opacity, as described later. The maps of the SO and  $\text{CH}_3\text{OH}$  lines show an intensity peak at the eastern and western parts, respectively, although these distributions have been reported to be similar in some protostellar sources, L1527 (Sakai et al. 2014b) and IRAS 15398-3359 (Okoda et al. 2020), as well as in some pre-stellar sources, L1554 (Spezzano et al. 2017) and L1521E (Nagy et al. 2019).

The data for the PCA are prepared as follows. As this source is known to have a small disk/envelope system, we focus on the distributions in the  $0''.5 \times 0''.5$  area around the protostar. The velocity range used for the data is from  $-0.2$  to  $14.5 \text{ km s}^{-1}$  ( $V_{\text{sys}} \sim 8.34 \text{ km s}^{-1}$ ; Yen et al. 2015) to cover the spectral feature in the above area, where the velocity channel width is  $0.7 \text{ km s}^{-1}$ . The velocity range is the same as that used for the moment 0 maps of Figure 3. For a fair comparison among the lines, we set the uniform beam size to be  $0''.034 \times 0''.034$ . These spatial area and velocity range correspond to  $100 \times 100$  pixels and 22 velocity channels, respectively.

The eigenvalues and eigenvectors of the first seven PCs are given in Table 3, where the molecular lines are ordered by PC1. PC1 shows the largest contribution ratio of 31.7%. The contribution ratios of the second and third principal components (PC2 and PC3) are 13.0% and 7.9%, respectively, and the fourth principal component (PC4) has a lower ratio of 5.0%. We here discuss PC1 and PC2, where the sum of the contribution ratios is 47.7%. The scree plot is shown in Figure 4, where the contribution ratios of the principal components to the original data are plotted. The elbow in the plot suggests how many PCs mainly contribute to the original data. Here, the molecular-line data can almost be reproduced by the first four PCs. PC3 and PC4 also extract some characteristic features of the molecular lines. Hence, they are briefly discussed in Appendix A.

### 3.3. Characteristic Features of the Principal Components

The moment 0 and channel maps of the first two PCs are shown in Figure 5. The moment 0 map of PC1 shows a round distribution around the protostar over  $\sim 30 \text{ au}$  (Figure 5(a)). It

**Table 2**  
Observed Molecular Lines for PCA<sup>a</sup>

Number	Molecule	Transition	Frequency (GHz)	$S\mu^2$ ( $D^2$ )	$E_u k^{-1}$ (K)	Original beam size	$\sigma$ (Cube) (mJy beam <sup>-1</sup> )	$\sigma$ (Moment 0) (mJy beam <sup>-1</sup> km s <sup>-1</sup> )	Bandwidth (MHz)	Resolution (kHz)
1	CH <sub>3</sub> OH	18 <sub>3,15</sub> – 18 <sub>2,16</sub> , A	247.610918	69.431	447	0″030 × 0″023 (P.A. –32°)	0.6	3	238	244
2	CH <sub>3</sub> OH	21 <sub>3,18</sub> – 21 <sub>2,19</sub> , A	245.223019	82.489	586	0″030 × 0″023 (P.A. –32°)	0.6	3	237	488
3	CH <sub>3</sub> OH	12 <sub>6,7</sub> – 13 <sub>5,8</sub> , E	261.704409	8.5234	360	0″029 × 0″022 (P.A. –29°)	0.6	3	238	489
4	CH <sub>3</sub> CHO	14 <sub>1,14</sub> – 13 <sub>1,13</sub> , A	260.5440195	175.9719	96	0″030 × 0″023 (P.A. –32°)	0.7	3	238	244
5	CH <sub>3</sub> OH	17 <sub>3,14</sub> – 17 <sub>2,15</sub> , A	248.282424	65.259	405	0″030 × 0″023 (P.A. –32°)	0.7	3	238	490
6	CH <sub>3</sub> OH	4 <sub>2,2</sub> – 5 <sub>1,5</sub> , A	247.228587	4.344	61	0″030 × 0″023 (P.A. –32°)	0.6	3	238	244
7	CH <sub>2</sub> DOH	4 <sub>2,2</sub> – 4 <sub>1,3</sub> , e <sub>0</sub>	244.8411349	2.54	38	0″030 × 0″023 (P.A. –32°)	0.6	3	237	488
8	CH <sub>2</sub> DOH	5 <sub>2,4</sub> – 5 <sub>1,5</sub> , e <sub>0</sub>	261.6873662	4.006	48	0″029 × 0″022 (P.A. –29°)	0.6	3	238	489
9	CH <sub>2</sub> DOH	3 <sub>2,1</sub> – 3 <sub>1,2</sub> , e <sub>0</sub>	247.6257463	2.36	29	0″030 × 0″023 (P.A. –32°)	0.6	3	238	244
10	CH <sub>3</sub> OH	2 <sub>1,1</sub> – 1 <sub>0,1</sub> , E	261.805675	5.336	28	0″029 × 0″022 (P.A. –29°)	0.6	3	238	489
11	HNCO	12 <sub>0,12</sub> – 11 <sub>0,11</sub>	263.748625	29.956	82	0″028 × 0″022 (P.A. –31°)	0.8	3	237	488
12	CS	5–4	244.9355565	19.2	35	0″030 × 0″023 (P.A. –32°)	0.5	3	237	488
13	NH <sub>2</sub> CHO	12 <sub>0,12</sub> – 11 <sub>0,11</sub>	247.390719	156.32	78	0″030 × 0″023 (P.A. –32°)	0.6	3	238	244
14	SO	$J_N = 7_6 - 6_5$	261.843721	16.4	48	0″029 × 0″022 (P.A. –29°)	0.6	3	238	489
15	CH <sub>2</sub> DOH	10 <sub>2,8</sub> – 10 <sub>1,9</sub> , o <sub>1</sub>	244.9888456	3.439	153	0″030 × 0″023 (P.A. –32°)	0.6	3	237	488
16	H <sub>2</sub> CO	10 <sub>1,9</sub> – 10 <sub>1,10</sub>	264.27014	3.1665	210	0″028 × 0″022 (P.A. –31°)	1.0	5	237	488
17	CHD <sub>2</sub> OH	$J = 6-5, K = 1+, o_1$	246.1432950	4.8216	53	0″030 × 0″023 (P.A. –32°)	0.6	3	237	488
18	HNCO	12 <sub>1,12</sub> – 11 <sub>1,11</sub>	262.7687626	29.413	125	0″029 × 0″022 (P.A. –31°)	0.7	3	238	489
19	HCOOH	11 <sub>5,7</sub> – 10 <sub>5,6</sub> and 11 <sub>5,6</sub> – 10 <sub>5,5</sub>	247.5139713	17.633	151	0″030 × 0″023 (P.A. –32°)	0.6	3	238	244
20	SO <sub>2</sub>	10 <sub>3,7</sub> – 10 <sub>2,8</sub>	245.5634219	14.513	73	0″030 × 0″023 (P.A. –32°)	0.6	3	238	244
21	HCOOH	12 <sub>0,12</sub> – 11 <sub>0,11</sub>	262.103481	24.157	83	0″029 × 0″022 (P.A. –29°)	0.6	3	238	244
22	CHD <sub>2</sub> OH	$J = 6-5, K = 1+, e_0$	246.2530390	4.7596	45	0″030 × 0″023 (P.A. –32°)	0.5	3	237	488
23	CH <sub>3</sub> CHO	14 <sub>0,14</sub> – 13 <sub>0,13</sub> , E, $v_t = 1$	263.8319277	175.5781	300	0″028 × 0″022 (P.A. –31°)	0.8	3	237	488
24	HCOOH	11 <sub>6,6</sub> – 10 <sub>6,5</sub> and 11 <sub>6,5</sub> – 10 <sub>6,4</sub>	247.4462429	15.614	186	0″030 × 0″023 (P.A. –32°)	0.6	3	238	244
25	CH <sub>3</sub> OD	5 <sub>1-4_0</sub> , E	245.142988	...	...	0″030 × 0″023 (P.A. –32°)	0.6	3	237	488
26	HC <sub>3</sub> N	27–26	245.6063199	375.98	165	0″030 × 0″023 (P.A. –32°)	0.6	3	238	244
27	CH <sub>3</sub> OCHO	21 <sub>7,14</sub> – 20 <sub>7,13</sub> , A	261.74658	99.483	170	0″029 × 0″022 (P.A. –29°)	0.5	3	238	489
28	C <sub>2</sub> H <sub>5</sub> OH	13 <sub>2,12</sub> – 12 <sub>1,11</sub>	262.1542443	12.186	81	0″029 × 0″022 (P.A. –29°)	0.7	3	238	244
29	CH <sub>3</sub> OCHO	21 <sub>7,14</sub> – 20 <sub>7,13</sub> , E	261.715518	97.5789	170	0″029 × 0″022 (P.A. –29°)	0.6	3	238	489
30	CH <sub>3</sub> COCH <sub>3</sub>	14 <sub>11,3</sub> – 13 <sub>10,4</sub>	264.2428888	126.0112	90	0″028 × 0″022 (P.A. –31°)	0.9	3	237	488
31	CH <sub>2</sub> OHCHO	7 <sub>7,1</sub> – 6 <sub>6,0</sub> and 7 <sub>7,0</sub> – 6 <sub>6,1</sub>	245.5362413	35.102	45	0″030 × 0″023 (P.A. –32°)	0.6	3	238	244
32	CH <sub>3</sub> OCHO	20 <sub>11,10</sub> – 19 <sub>11,9</sub> , E	246.308272	74.4142	204	0″030 × 0″023 (P.A. –32°)	0.6	3	237	488

**Note.**

<sup>a</sup> Line parameters are taken from CDMS (Endres et al. 2016) and JPL (Pickett et al. 1998) except for CH<sub>3</sub>OD. <sup>b</sup> The parameter for CH<sub>3</sub>OD is taken from Duan et al. (2003). The rms noise ( $\sigma$ ) and the beam size are based on the observation data. The spectral bandwidth and the channel width are taken from the header of each image data. The molecular lines are ordered by PC1 of PCA-3D in Table 3 for consistency in the numbering of molecular lines.

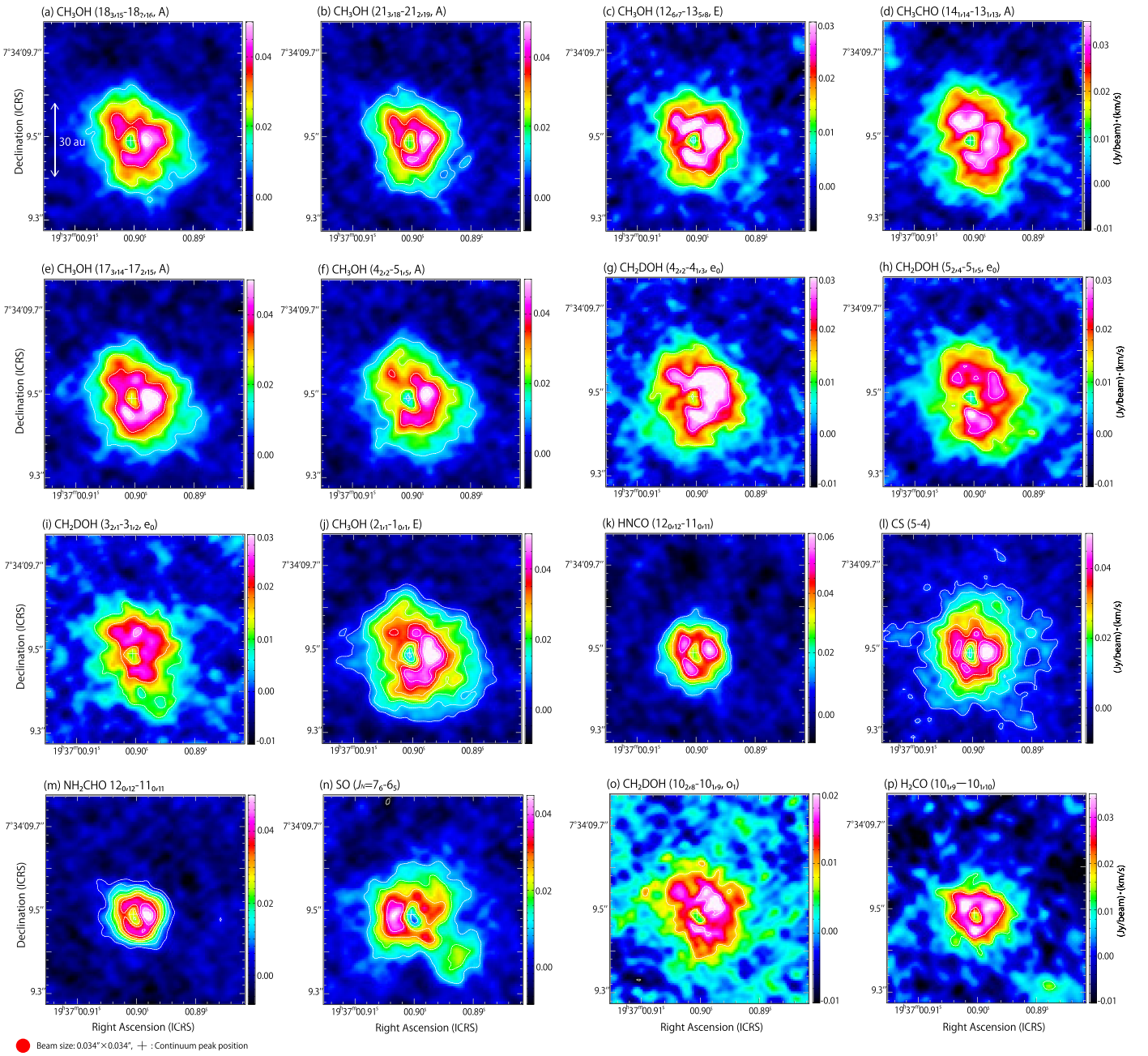


**Figure 3.** Moment 0 maps of the 32 molecular lines, which are used in PCA-3D. A uniform spatial resolution of  $0''.034 \times 0''.034$  is applied for these images. The cross marks show the continuum peak position:  $(\alpha_{2000}, \delta_{2000}) = (19^{\text{h}}37^{\text{m}}00^{\text{s}}.90, +7^{\circ}34'09''.49)$ . The order of (a)–(af) is the same as that in Table 2 (1–32). The integrated velocity range is from  $-0.2$  to  $14.5 \text{ km s}^{-1}$ . Contour levels are every  $3\sigma$  from  $3\sigma$ , where  $\sigma$  is listed in Table 2.

slightly extends toward the southwest direction with an intensity depression at the continuum peak position. In its velocity channel maps, the distribution of PC1 is clearly seen in the panels from  $5.4$  to  $11 \text{ km s}^{-1}$  (Figure 5(c)). The blueshifted and redshifted components can be seen mainly in the southeast and the northwest, respectively, where the systemic velocity is  $8.34 \text{ km s}^{-1}$  (Yen et al. 2015). This slight gradient can be interpreted as a rotating motion, as pointed out by Imai et al. (2019) and Bjerkeli et al. (2019). Figures 6(a) and (b) show a position–velocity (PV) diagram of PC1 along the envelope (P.A.  $0^\circ$ ) and outflow (P.A.  $90^\circ$ ) directions, respectively. For the envelope direction, the diamond shape is seen in the velocity structure (Figure 6(a)), which is characteristic of the infalling–rotating motion, as reported previously (e.g.,

Ohashi et al. 1997; Sakai et al. 2014b; Oya et al. 2016). This result is consistent with the report by Imai et al. (2019). On the other hand, in the  $9.6$  and  $11.0 \text{ km s}^{-1}$  panels of Figure 5(c), we can see the intensity peak at the northwestern side of the continuum peak. As the eastern side of the disk/envelope system faces us, the enhancement of the northwestern part is not explained by the inclination effect obscuring the emission from the backside: the eastern part of the disk/envelope structure should be more bright, if its inclination angle is considered. According to Bjerkeli et al. (2019), the SiO emission traces the foot of the outflow and has an intensity peak at the western part of about  $0''.03$  from the continuum peak. It is reported to be shocked region caused by the outflow impact (Bjerkeli et al. 2019). Hence, the velocity structure of

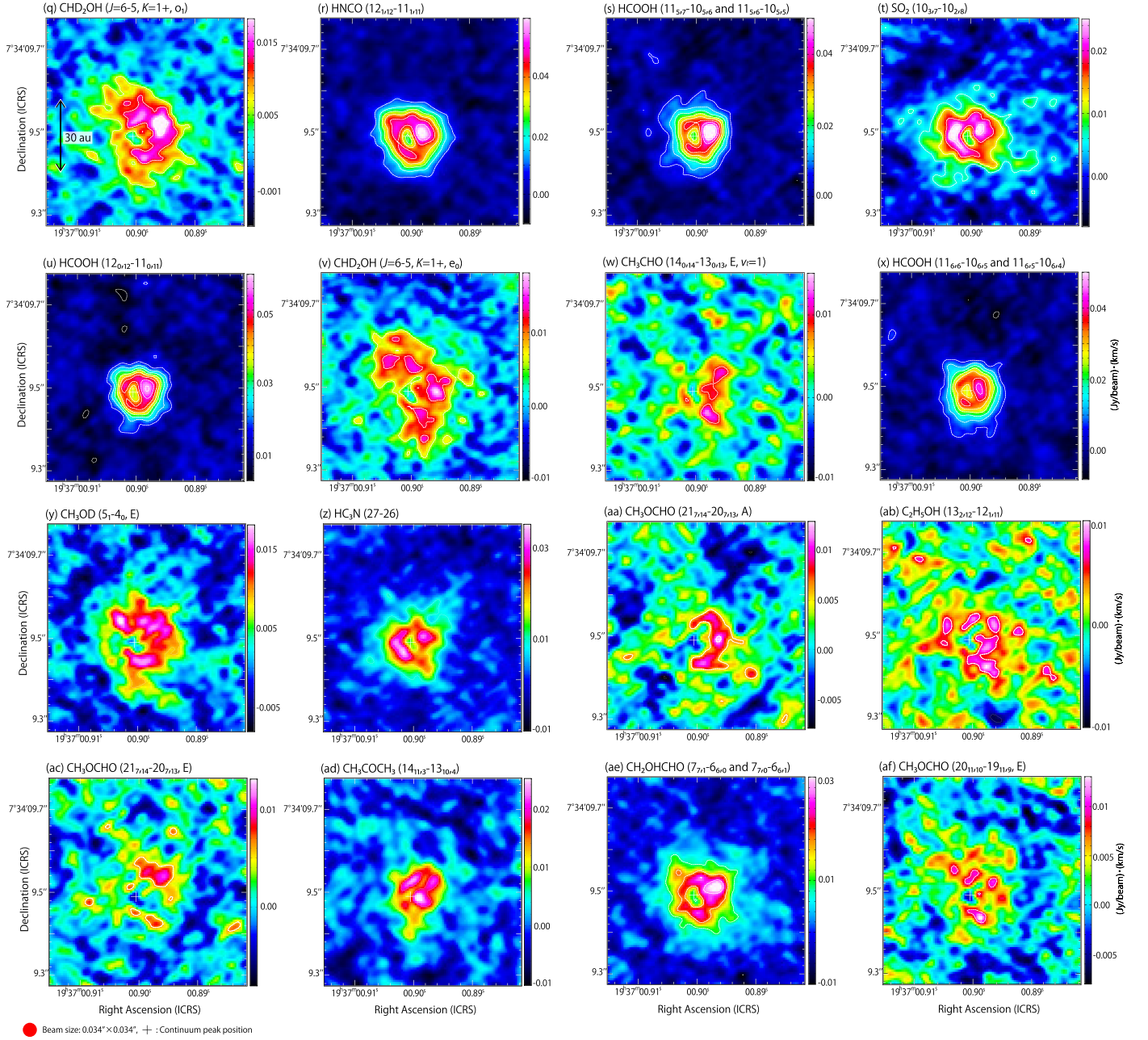


Figure 3. (Continued.)

PC1 would also be affected by the outflow motion. This sign can also be confirmed in the PV diagram along the outflow direction (Figure 6(b)). The velocity seems to be higher with increasing distance from the continuum peak on the western side. Figure 7 shows the spectral line profiles of PC1 and PC2, which are prepared for a circular region with a diameter of  $0''.1$  centered at the continuum peak. The spectrum of PC1 reveals a single peak at the slightly blueshifted velocity (Figure 7(a)).

As shown in Figure 5(b), the moment 0 map of PC2 shows a positive compact distribution in the vicinity of the protostar as well as the negative crescent distribution around it. Note that the PCA process yields such a negative distribution in some PCs, because we look for the orthogonal axes for molecular-line distributions in the process. Its distribution is also seen clearly in the velocity channel map of PC2 (Figure 5(d)). The spectral line profile of PC2 has a positive double-peak feature

with a dip of  $\sim 6 \text{ km s}^{-1}$  (Figure 7(b)), where the positive compact distribution has a broader velocity width than in PC1. PC2 reproduces high-velocity components of the molecular lines in combination with PC1. The molecular lines having such a feature are described in the next subsection.

### 3.4. Characteristics of the Molecular Lines Extracted by the PCA

Figures 8(a) and (b) show the correlation coefficients between the principal components and the cube data for each molecular line, by using the method described previously (Okoda et al. 2020, 2021). The numbers for the molecular lines are assigned in decreasing order of the PC1 value. In Figure 8(a), 19 molecular lines have a correlation coefficient larger than 0.5 for PC1, where the high-excitation  $\text{CH}_3\text{OH}$  lines

**Table 3**  
Eigenvectors of the Principal Components and Their Eigenvalues for PCA-3D<sup>a</sup>

Number	Molecule	PC1	PC2	PC3	PC4	PC5	PC6	PC7
1	CH <sub>3</sub> OH (18 <sub>3,15</sub> – 18 <sub>2,16</sub> , A)	0.276	–0.007	–0.123	0.064	0.089	0.012	0.037
2	CH <sub>3</sub> OH (21 <sub>3,18</sub> – 21 <sub>2,19</sub> , A)	0.269	0.029	0.021	0.041	–0.083	0.006	0.030
3	CH <sub>3</sub> OH (12 <sub>6,7</sub> – 13 <sub>5,8</sub> , E)	0.261	–0.056	0.064	–0.102	0.003	–0.069	0.034
4	CH <sub>3</sub> CHO (14 <sub>1,14</sub> – 13 <sub>1,13</sub> , A)	0.240	–0.112	0.092	–0.091	–0.090	–0.041	–0.126
5	CH <sub>3</sub> OH (17 <sub>3,14</sub> – 17 <sub>2,15</sub> , A)	0.240	–0.008	–0.211	0.145	0.044	0.054	–0.124
6	CH <sub>3</sub> OH (4 <sub>2,2</sub> – 5 <sub>1,5</sub> , A)	0.235	0.008	–0.241	0.038	–0.031	0.117	0.004
7	CH <sub>2</sub> DOH (4 <sub>2,2</sub> – 4 <sub>1,3</sub> , e <sub>0</sub> )	0.234	–0.176	0.048	0.020	–0.021	0.013	0.017
8	CH <sub>2</sub> DOH (5 <sub>2,4</sub> – 5 <sub>1,5</sub> , e <sub>0</sub> )	0.230	–0.161	–0.043	0.005	0.090	–0.083	–0.096
9	CH <sub>2</sub> DOH (3 <sub>2,1</sub> – 3 <sub>1,2</sub> , e <sub>0</sub> )	0.224	–0.170	0.037	–0.021	0.129	–0.091	–0.178
10	CH <sub>3</sub> OH (2 <sub>1,1</sub> – 1 <sub>0,1</sub> , E)	0.208	–0.027	–0.314	–0.014	–0.191	0.030	–0.184
11	HNCO (12 <sub>0,12</sub> – 11 <sub>0,11</sub> )	0.202	0.263	0.012	–0.077	–0.042	–0.063	0.135
12	CS (5–4)	0.192	–0.032	–0.270	0.020	0.003	–0.041	0.137
13	NH <sub>2</sub> CHO (12 <sub>0,12</sub> – 11 <sub>0,11</sub> )	0.188	0.322	0.136	–0.058	0.053	0.034	0.009
14	SO ( <i>J<sub>N</sub></i> = 7 <sub>6</sub> – 6 <sub>5</sub> )	0.176	0.041	–0.247	0.136	–0.061	–0.229	0.186
15	CH <sub>2</sub> DOH (10 <sub>2,8</sub> – 10 <sub>1,9</sub> , o <sub>1</sub> )	0.159	–0.184	0.214	–0.142	–0.116	0.156	0.067
16	H <sub>2</sub> CO (10 <sub>1,9</sub> – 10 <sub>1,10</sub> )	0.159	0.056	0.207	–0.138	0.067	0.111	0.006
17	CHD <sub>2</sub> OH ( <i>J</i> = 6–5, <i>K</i> = 1+, o <sub>1</sub> )	0.159	–0.207	0.082	–0.089	0.118	0.258	0.042
18	HNCO (12 <sub>1,12</sub> – 11 <sub>1,11</sub> )	0.157	0.176	–0.168	0.038	–0.071	0.187	0.065
19	HCOOH (11 <sub>5,7</sub> – 10 <sub>5,6</sub> and 11 <sub>5,6</sub> – 10 <sub>5,5</sub> )	0.156	0.279	0.117	0.008	0.128	0.242	–0.027
20	SO <sub>2</sub> (10 <sub>3,7</sub> – 10 <sub>2,8</sub> )	0.155	0.211	0.077	0.144	–0.134	–0.38	0.126
21	HCOOH(12 <sub>0,12</sub> – 11 <sub>0,11</sub> )	0.145	0.282	0.230	–0.200	0.082	0.027	–0.029
22	CHD <sub>2</sub> OH ( <i>J</i> = 6–5, <i>K</i> = 1+, e <sub>0</sub> )	0.134	–0.251	0.167	0.092	0.036	0.031	0.064
23	CH <sub>3</sub> CHO (14 <sub>0,14</sub> – 13 <sub>0,13</sub> , E, <i>v<sub>t</sub></i> = 1)	0.122	–0.179	–0.132	–0.293	–0.139	–0.146	–0.366
24	HCOOH (11 <sub>6,6</sub> – 10 <sub>6,5</sub> and 11 <sub>6,5</sub> – 10 <sub>6,4</sub> )	0.119	0.287	0.283	–0.132	0.105	0.012	–0.015
25	CH <sub>3</sub> OD (5 <sub>1,4</sub> , E)	0.118	–0.278	0.165	0.278	0.019	0.042	0.129
26	HC <sub>3</sub> N (27–26)	0.114	0.268	–0.07	0.278	–0.055	–0.071	0.142
27	CH <sub>3</sub> OCHO (21 <sub>7,14</sub> – 20 <sub>7,13</sub> , A)	0.114	–0.265	0.217	0.032	0.236	0.025	0.451
28	C <sub>2</sub> H <sub>5</sub> OH (13 <sub>2,12</sub> – 12 <sub>1,11</sub> )	0.089	0.048	0.274	0.381	–0.245	–0.044	–0.319
29	CH <sub>3</sub> OCHO (21 <sub>7,14</sub> – 20 <sub>7,13</sub> , E)	0.048	–0.028	0.094	–0.537	–0.420	–0.123	0.043
30	CH <sub>3</sub> COCH <sub>3</sub> (14 <sub>1,3</sub> – 13 <sub>10,4</sub> )	0.034	0.008	0.170	0.136	0.395	–0.234	–0.520
31	CH <sub>2</sub> OHCHO (7 <sub>7,1</sub> – 6 <sub>6,0</sub> and 7 <sub>7,0</sub> – 6 <sub>6,1</sub> )	0.016	0.093	–0.232	–0.095	0.215	0.557	–0.156
32	CH <sub>3</sub> OCHO (20 <sub>11,10</sub> – 19 <sub>11,9</sub> , E)	–0.019	–0.022	0.213	0.294	–0.545	0.384	–0.115
Eigenvalues		10.27	4.212	2.549	1.618	1.482	1.242	1.165
Contribution ratio (%)		31.7	13.0	7.9	5.0	4.6	3.8	3.6

**Note.**

<sup>a</sup> These values are also called “loadings”.

and most of the CH<sub>2</sub>DOH lines show the largest values. This suggests that most molecular lines have a similar distribution to PC1, which is a roundly extended distribution around the protostar with an intensity depression at the continuum peak. Based on the velocity structure of PC1 (Figures 5(c) and 6(a)), these lines reveal a rotating structure of the disk/envelope system.

Figure 8(b) depicts the correlation between PC2 and each molecular line. While the CH<sub>3</sub>OH lines showing the large correlation for PC1 (#1, #2, #3, #5, #6, and #10) are not well correlated with PC2, the nitrogen-bearing organic species, NH<sub>2</sub>CHO (#13), HNCO (#11 and #18), and HC<sub>3</sub>N (#26), have a positive correlation for PC2. This indicates different distributions between the oxygen-bearing and nitrogen-bearing species. Furthermore, the HCOOH lines (#19, #21, and #24) have a large positive correlation for PC2 and show a similar trend to the nitrogen-bearing molecular lines, despite an oxygen-bearing species. A positive large correlation of PC2 means the compact distribution with the high-velocity component of these molecular lines. Additionally, the SO<sub>2</sub> line (#20) is also correlated with PC2 positively, indicating that its distribution is more compact than those of the oxygen-bearing organic species (Figure 3(t)). In contrast, the deuterated species

of CH<sub>3</sub>OH (CH<sub>2</sub>DOH: #7, #8, #9, and #15, CHD<sub>2</sub>OH: #17 and #22, and CH<sub>3</sub>OD: #25), CH<sub>3</sub>OCHO (#27), and CH<sub>3</sub>CHO (#4 and #23) lines are correlated with PC2 negatively. This result indicates that they have a more extended distribution around the protostar. In particular, it is remarkable that the moment 0 map of CH<sub>3</sub>OD (#25) resembles the negative crescent of PC2 (Figure 3(y)). In short, the molecular lines with a negative correlation for PC2 have an extended distribution, resulting in their narrow line width.

An unbiased classification of the molecular lines can be done in the PC1–PC2 biplot of Figure 8(c), which shows the contributions of the principal components for each molecular-line distribution. The cyan, blue, and light blue plots represent, CH<sub>3</sub>OH, deuterated CH<sub>3</sub>OH (CH<sub>2</sub>DOH, CHD<sub>2</sub>OH, and CH<sub>3</sub>OD), and the other oxygen-bearing organic molecules, respectively. The yellow plots indicate the nitrogen-bearing molecules. The PC2 contributions of the nitrogen-bearing molecules tend to be larger than those of the oxygen-bearing ones except for HCOOH (#19, #21, and #24), indicating the compact distribution of the nitrogen-bearing ones. Thus, the positive and negative PC2 contributions clearly reveal the systemic differentiation between the nitrogen-bearing and oxygen-bearing molecules.

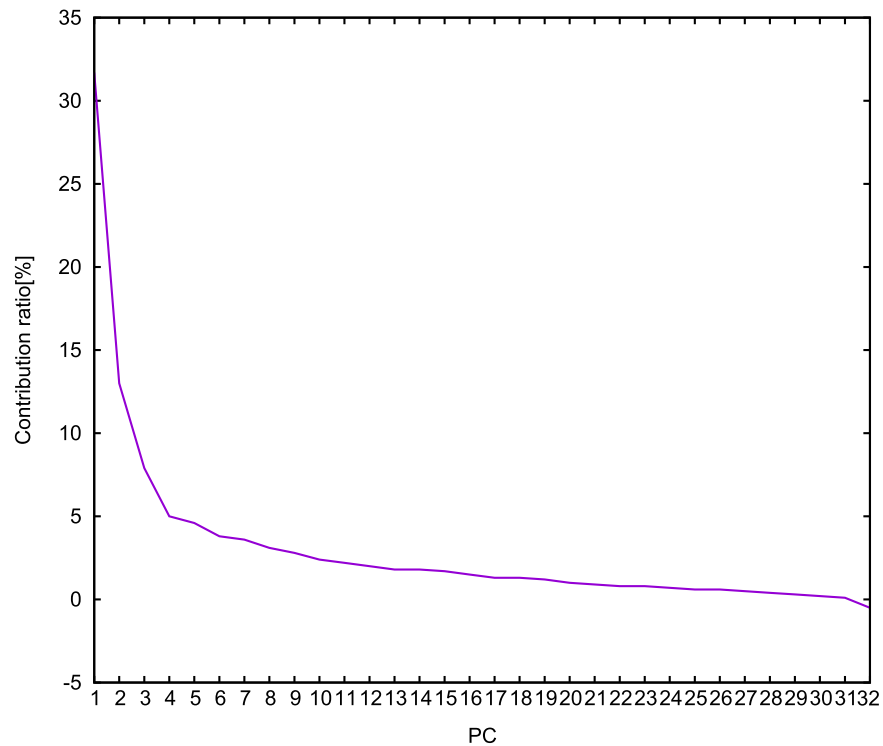


**Figure 4.** Scree plots of the contribution ratios of the principal components. The elbow seen at PC4 in the plot suggests that the first four PCs mainly contribute to the original data. In other words, the molecular-line data can almost be reproduced by only the first four PCs.

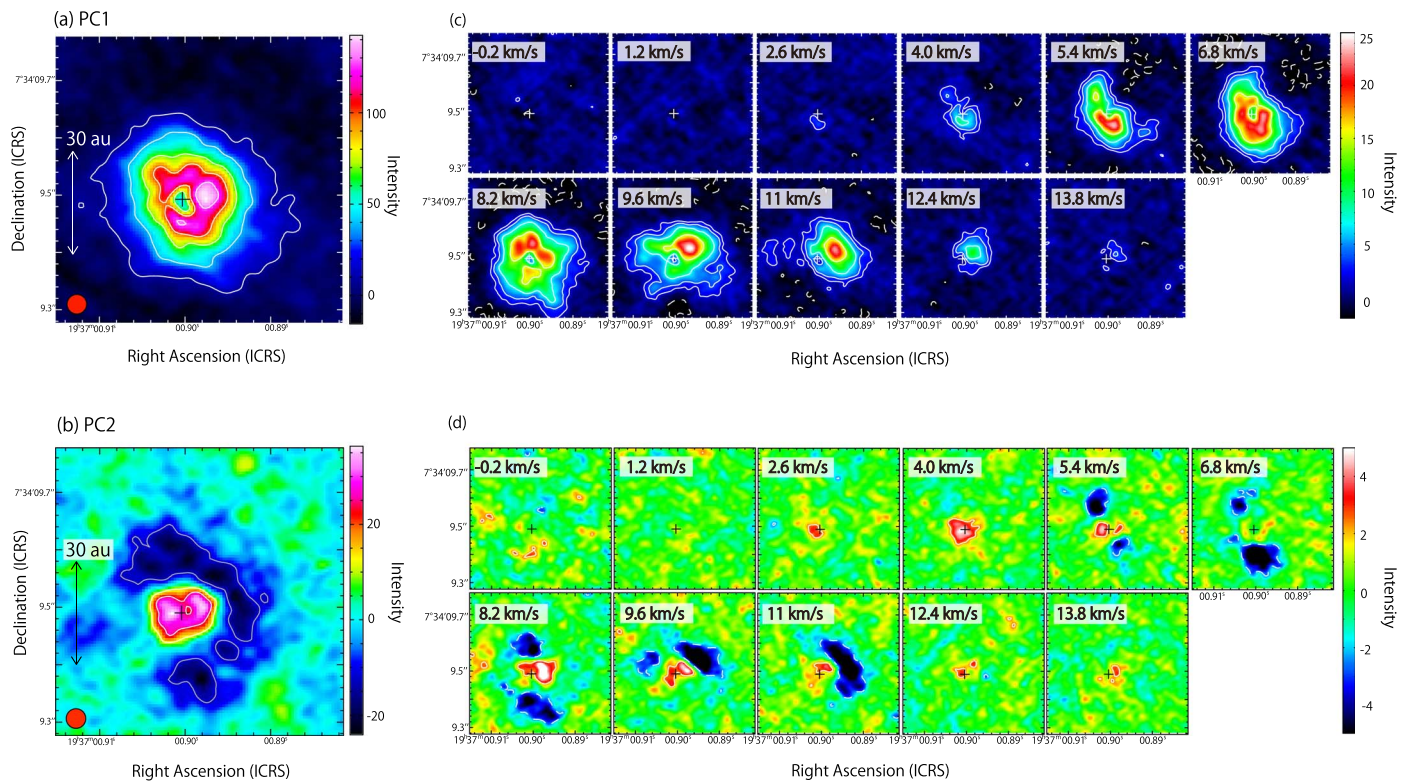


**Figure 5.** (a), (b) Moment 0 maps of the first two principal components in PCA-3D. The velocity range of integration is from  $-0.2$  to  $14.5 \text{ km s}^{-1}$ . Contour levels for PC1 (a) are every  $10\sigma$  from  $3\sigma$ , where  $\sigma$  is 3, and those for PC2 (b) are every  $3\sigma$  from  $3\sigma$ , where  $\sigma$  is 4. The red circles show the beam size. (c), (d) Channel maps of the first two principal components. Each panel represents the integrated intensity over a velocity range of  $1.4 \text{ km s}^{-1}$  except for the last one (the panel of  $13.8 \text{ km s}^{-1}$ ), whose lower-end velocity is quoted on the upper-left corner. The panel of  $13.8 \text{ km s}^{-1}$  is integrated over a velocity range of  $0.7 \text{ km s}^{-1}$ . The systemic velocity is  $8.34 \text{ km s}^{-1}$ . Contour levels for PC1 (c) and PC2 (d) are every  $3\sigma$  from  $3\sigma$ , where  $\sigma$  is 0.6 and 0.8, respectively. The cross marks show the continuum peak position.

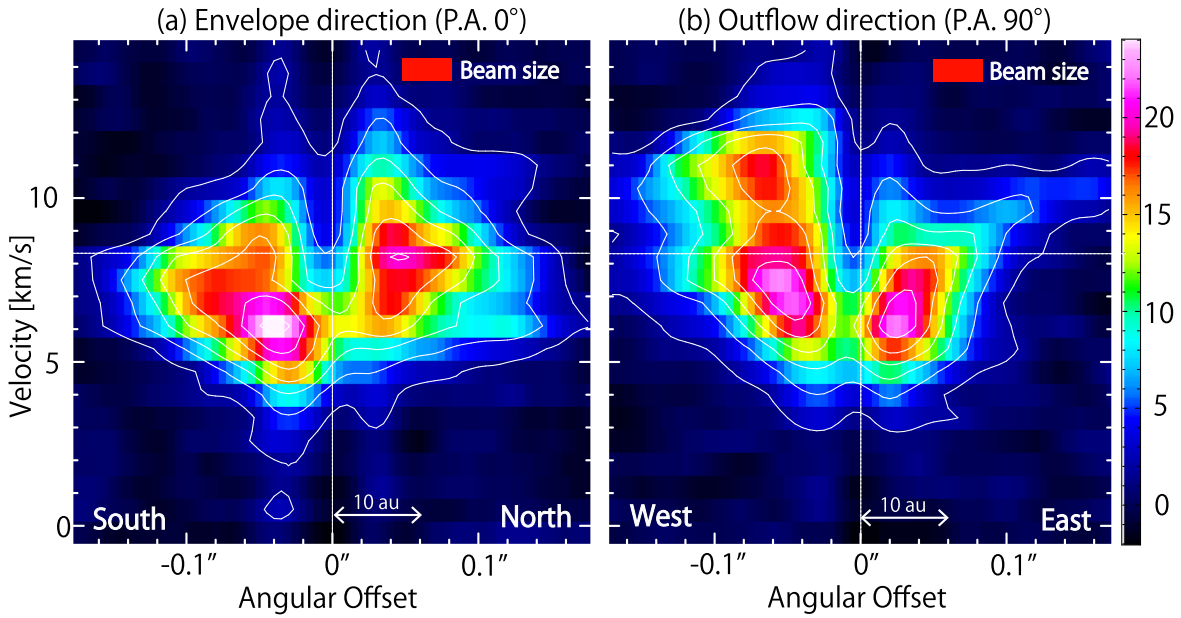


**Figure 6.** Position–velocity diagrams of PC1 along the envelope (a) and outflow (b) directions (Figure 1). The horizontal dotted lines represent the systemic velocity of  $8.34 \text{ km s}^{-1}$ . The horizontal axis represents the angular offset from the continuum peak. Contour levels are every  $3\sigma$  from  $3\sigma$ , where  $\sigma$  is 0.6.

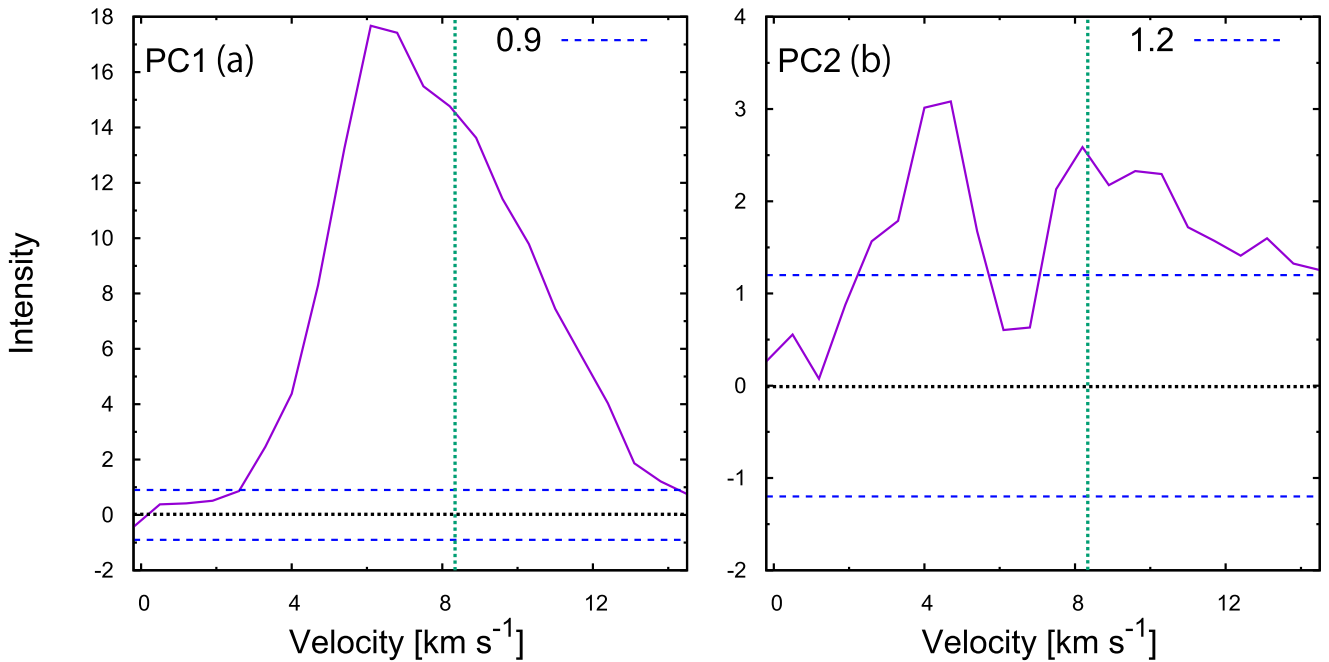


**Figure 7.** Spectral line profiles of the first two principal components in PCA-3D. The spectra are prepared for a circular region within a diameter of  $0''.1$  centered at the continuum peak. The horizontal blue dashed lines represent  $\pm 3\sigma$  noise levels, where  $\sigma$  for (a) PC1 and (b) PC2 is 0.3 and 0.4, respectively. The horizontal black dotted lines represent the zero-level intensity. The vertical green dotted lines represent the systemic velocity of  $8.34 \text{ km s}^{-1}$ .

Furthermore, a small systematic difference between  $\text{CH}_3\text{OH}$  and its deuterated species can be seen in the plot (Figure 8(c)). The deuterated species tend to have a larger negative contribution of PC2, indicating a more extended distribution with a narrower line width than  $\text{CH}_3\text{OH}$ . Although their extended features can be recognized by eye in the moment 0 maps (Figure 3), we can show it by the PCA-3D definitively in an unbiased way.

We reveal the molecular-line distributions systematically by using PCA. The trend for the oxygen-bearing and nitrogen-bearing species is extracted as in the case of PCA-3D in L483 reported by Okoda et al. (2021), and the HCOOH lines are

found to show a similar trend to the nitrogen-bearing molecules,  $\text{NH}_2\text{CHO}$ , HNC, and  $\text{HC}_3\text{N}$ .

#### 4. Temperature Distribution

In Section 3, PCA-3D reveals that the distributions of HCOOH and  $\text{NH}_2\text{CHO}$  are more compact than those of  $\text{CH}_3\text{OH}$  and  $\text{CH}_2\text{DOH}$ . As the first step to exploring the chemical processes, it is essential to derive the gas temperature in the disk/envelope system. We select the four species, HCOOH,  $\text{NH}_2\text{CHO}$ ,  $\text{CH}_2\text{DOH}$ , and  $\text{CH}_3\text{OH}$ , for this purpose because multiple lines are detected for each of them. The

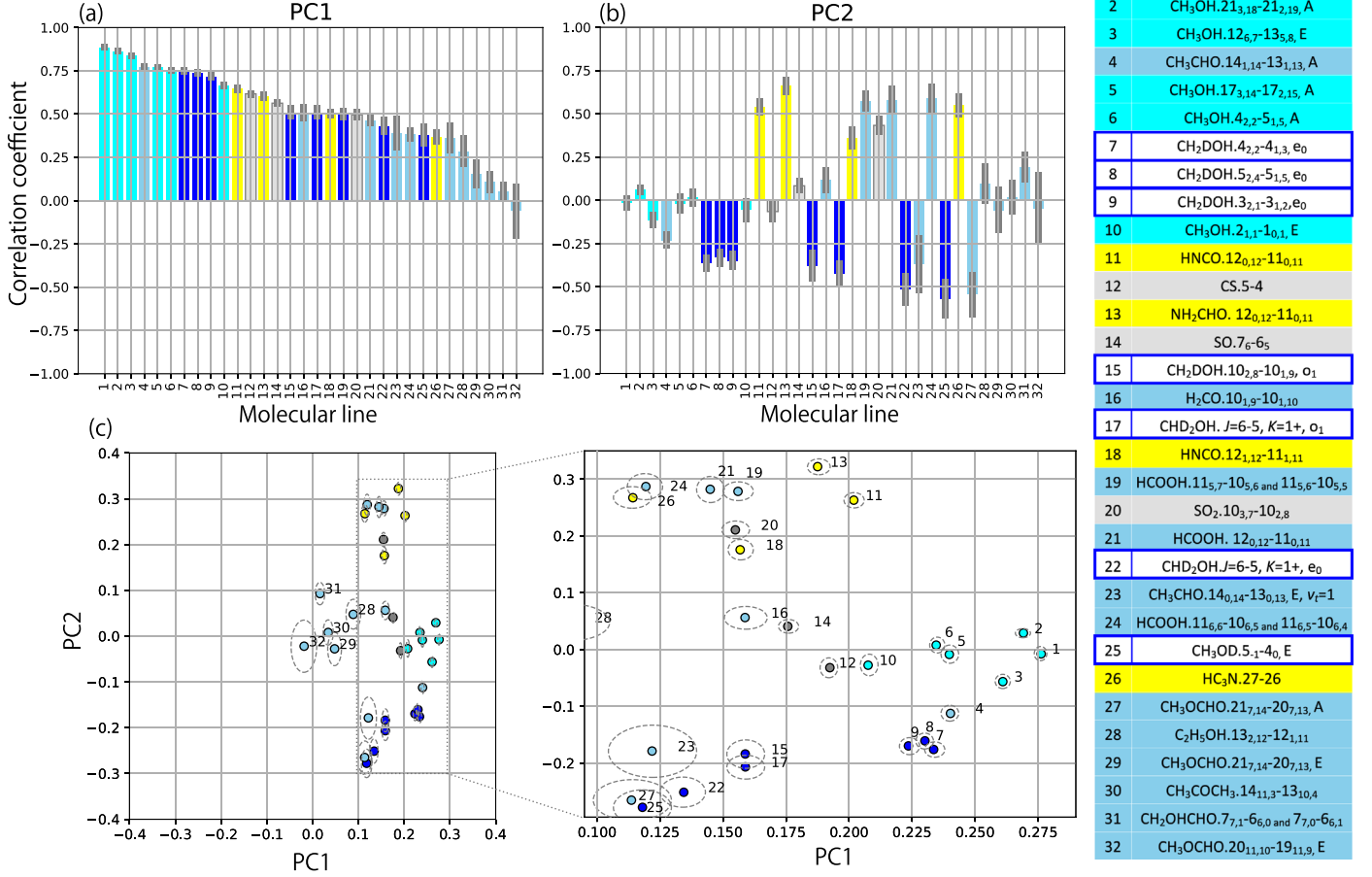


**Figure 8.** (a), (b) Correlation coefficients between the first two principal components in PCA-3D and the molecular lines. The uncertainties are shown in gray, which are evaluated by the method reported by Okoda et al. (2020, 2021). The numbers represent the molecular lines listed in the attached table. (c) Biplots of the contributions for the principal components in PCA-3D for each molecular-line distribution on the PC1–PC2 plane. The dashed ellipses represent the uncertainties, which are evaluated by the method reported by Okoda et al. (2020, 2021). The numbers represent the molecular lines listed in the attached table. Cyan, blue, and light blue plots represent CH<sub>3</sub>OH, deuterated CH<sub>3</sub>OH (CH<sub>2</sub>DOH, CHD<sub>2</sub>OH, and CH<sub>3</sub>OD), and the other oxygen-bearing molecules, respectively. Yellow plots indicate the nitrogen-bearing organic molecules.

molecular lines for the derivation are listed in Table 4. In this analysis, we add some lines of HCOOH and NH<sub>2</sub>CHO, which are not used in PCA due to their weak intensities and proximity to adjacent lines. We derive the rotation temperature at the positions along the envelope direction in Figure 1(b).

#### 4.1. Derivation of Temperature

The rotation temperatures at the nine positions (positions 1–8 of Figure 1(b) and the continuum peak position) along the envelope direction are derived under the assumption of local thermodynamic equilibrium (LTE) from the observed intensities and the velocity widths of the HCOOH, NH<sub>2</sub>CHO, CH<sub>2</sub>DOH, and CH<sub>3</sub>OH lines (Table 4). As the dust emission is bright particularly toward the protostar position, we explicitly consider the effect of the optical depth of the dust emission ( $\tau_{\text{dust}}$ ) as well as that of the line emission ( $\tau_{\text{line}}$ ). For simplicity, we assume the condition that gas and dust are well mixed and the gas temperature is equal to the dust temperature. In this case, the observed intensity ( $T_{\text{obs}}$ ) is represented as follows

based on radiative transfer:

$$T_{\text{obs}} = \frac{c^2}{2\nu^2 k_B} [B_\nu(T) + \exp\{-\tau_{\text{line}} + \tau_{\text{dust}}\}] \times \{B_\nu(T_{\text{cb}}) - B_\nu(T)\} - I_{\text{dust}}, \quad (1)$$

where  $B_\nu(T)$  and  $B_\nu(T_{\text{cb}})$  are the Planck function for the source temperature at  $T$  and the cosmic microwave background temperature  $T_{\text{cb}}$ , respectively.  $\tau_{\text{line}}$  represents the optical depth of the molecular line, which can be written under the assumption of LTE as:

$$\tau_{\text{line}} = \frac{8\pi^3 S \mu^2}{3h \Delta\nu U(T)} \left\{ \exp\left(\frac{h\nu}{k_B T}\right) - 1 \right\} \exp\left(-\frac{E_u}{k_B T}\right) N, \quad (2)$$

where  $S$  is the line strength,  $\mu$  is the dipole moment responsible for the transition,  $h$  is the Planck constant,  $\Delta\nu$  is the FWHM in velocity,  $U(T)$  is the partition function of the molecule at the source temperature  $T$ ,  $\nu$  is the frequency,  $E_u$  is the upper-state energy, and  $N$  is the column density. On the other hand, the intensity of the dust continuum emission ( $I_{\text{dust}}$ ) near the line

**Table 4**  
Molecular Lines for the Derivation of the Temperature<sup>a</sup>

Molecule	Transition	Frequency (GHz)	$S\mu^2$ ( $D^2$ )	$E_{uk}^{-1}$ (K)	Beam Size	$\sigma$ (mJy beam <sup>-1</sup> ·km s <sup>-1</sup> )
HCOOH	11 <sub>6,6</sub> –10 <sub>6,5</sub>	247.4462429 <sup>b</sup>	15.614	186	0''030 × 0''023 (P.A. –32°)	3
	11 <sub>6,5</sub> –10 <sub>6,4</sub>	247.4462439 <sup>b</sup>	15.614	186		
	11 <sub>5,7</sub> –10 <sub>5,6</sub>	247.5139713 <sup>b</sup>	17.633	151	0''030 × 0''023 (P.A. –32°)	3
	11 <sub>5,6</sub> –10 <sub>5,5</sub>	247.5141176 <sup>b</sup>	17.633	151		
	11 <sub>3,8</sub> –10 <sub>3,7</sub>	248.2744893	20.573	100	0''030 × 0''023 (P.A. –31°)	2
NH <sub>2</sub> CHO	12 <sub>0,12</sub> –11 <sub>0,11</sub>	262.1034810	24.157	83	0''029 × 0''022 (P.A. –29°)	3
	13 <sub>0,13</sub> –12 <sub>1,12</sub>	244.8542130	6.6085	91	0''030 × 0''023 (P.A. –32°)	2
	12 <sub>0,12</sub> –11 <sub>0,11</sub> , $\nu_{12} = 1$	247.3273220	156.34	494	0''030 × 0''023 (P.A. –32°)	2
CH <sub>2</sub> DOH	12 <sub>0,12</sub> –11 <sub>0,11</sub>	247.3907190	156.32	78	0''030 × 0''023 (P.A. –32°)	2
	4 <sub>2,2</sub> –4 <sub>1,3</sub> , e <sub>0</sub>	244.8411349	2.540	38	0''030 × 0''023 (P.A. –32°)	2
	10 <sub>2,8</sub> –10 <sub>1,9</sub> , o <sub>1</sub>	244.9888456	3.439	153	0''030 × 0''023 (P.A. –32°)	2
CH <sub>3</sub> OH	3 <sub>2,1</sub> –3 <sub>1,2</sub> , e <sub>0</sub>	247.6257463	2.360	29	0''030 × 0''023 (P.A. –32°)	2
	5 <sub>2,4</sub> –5 <sub>1,5</sub> , e <sub>0</sub>	261.6873662	4.006	48	0''029 × 0''022 (P.A. –29°)	3
	21 <sub>3,18</sub> –21 <sub>2,19</sub> , A	245.2230190	82.489	586	0''030 × 0''023 (P.A. –32°)	3
	4 <sub>2,2</sub> –5 <sub>1,5</sub> , A	247.2285870	4.3444	61	0''030 × 0''023 (P.A. –32°)	3
	18 <sub>3,15</sub> –18 <sub>2,16</sub> , A	247.6109180	69.431	447	0''030 × 0''023 (P.A. –32°)	3
	17 <sub>3,14</sub> –17 <sub>2,15</sub> , A	248.2824240	65.259	405	0''030 × 0''023 (P.A. –31°)	3
	12 <sub>6,7</sub> –13 <sub>5,8</sub> , E	261.7044090	8.5234	360	0''029 × 0''022 (P.A. –29°)	3
2 <sub>1,1</sub> –1 <sub>0,1</sub> , E	261.8056750	5.336	28	0''029 × 0''022 (P.A. –29°)	3	

#### Notes.

<sup>a</sup> Line parameters are taken from CDMS (Endres et al. 2016) and JPL (Pickett et al. 1998). The rms noise ( $\sigma$ ) and the beam size are based on the observation data.

<sup>b</sup> Blended.

frequency is given as:

$$I_{\text{dust}} = B_{\nu}(T) + \exp(-\tau_{\text{dust}})[B_{\nu}(T_{\text{cb}}) - B_{\nu}(T)]. \quad (3)$$

Then, if the source temperature ( $T$ ) is derived from the multiline analysis, we obtain  $\tau_{\text{dust}}$  from  $I_{\text{dust}}$  as:

$$\tau_{\text{dust}} = -\ln \left\{ \frac{B_{\nu}(T) - I_{\text{dust}}}{B_{\nu}(T) - B_{\nu}(T_{\text{cb}})} \right\}. \quad (4)$$

If we assume that  $B_{\nu}(T) \gg B_{\nu}(T_{\text{cb}})$ , we have:

$$\tau_{\text{dust}} \sim -\ln \left\{ \frac{B_{\nu}(T) - I_{\text{dust}}}{B_{\nu}(T)} \right\}. \quad (5)$$

Based on these equations, we fit the observed intensities of each molecule at each position by using a nonlinear least-squares method to determine the rotation temperature ( $T$ ) and the molecular column density ( $N$ ). An example of the calculation results is shown in Appendix B.

#### 4.2. Temperature Distribution along the Disk/envelope System

The intensity profiles of the molecular lines along the envelope direction (Figure 1(a)) are shown in Figure 9(a). The intensity depression at the continuum peak is due to the high dust opacity. The distributions of HCOOH and NH<sub>2</sub>CHO are more compact than those of CH<sub>3</sub>OH and CH<sub>2</sub>DOH, as revealed by the PCA-3D results (Section 3.4). Hence, we derive the rotation temperatures within the offset of 0''06 for all molecules. As CH<sub>3</sub>OH and CH<sub>2</sub>DOH are extended outside that radius, we also calculate the temperatures for the positions up to the offset of 0''13 to the north and the south. The results are summarized in Table 5, where the errors are the fitting errors in the least-squares analysis. Examples of the fit at the positions of  $\pm 0''06$  are shown in Table 7 of Appendix B. The line optical depth is rather high, so that the column density has a large uncertainty. In contrast, the rotation

temperature is well constrained. The derived  $\tau_{\text{dust}}$  for the four lines are also summarized in Table 8 of Appendix B. It is derived to be 1.1–1.4 at the continuum peak at most.

Figure 9(b) shows the plot of the derived rotation temperatures along the envelope direction, where the colors represent the molecules: orange, green, yellow, and blue circles denote the rotation temperatures for HCOOH, NH<sub>2</sub>CHO, CH<sub>2</sub>DOH, and CH<sub>3</sub>OH, respectively. The error bar is shown for each value, and the purple line represents the intensity profiles of the 1.2 mm continuum, whose brightness temperature is 141 K at its peak position.

For all four molecules, the derived rotation temperature is the highest at the continuum peak position, which is in the range of 193–215 K, and decreases as an increasing distance from the protostar. Such a high temperature toward the continuum peak is often seen in hot corino sources (e.g., Watanabe et al. 2017; Jørgensen et al. 2018; Bianchi et al. 2020; De Simone et al. 2020; Oya & Yamamoto 2020). The temperatures are 154–195 K at the positions of  $\pm 0''03$  for the four molecules. These temperatures are roughly consistent with that expected from the protostellar luminosity of 1.6  $L_{\odot}$ . However, at the positions of  $\pm 0''06$ , the temperatures are remarkably different among the molecules. While CH<sub>3</sub>OH and CH<sub>2</sub>DOH show the high temperature of 150–165 K both in the south and north sides, the temperatures of HCOOH and NH<sub>2</sub>CHO are 75–76 and 112 K, respectively. The latter two are significantly lower than the former two. Namely, the temperatures of HCOOH and NH<sub>2</sub>CHO, which have a more compact distribution, decrease more steeply with increasing distance from the protostar than those of CH<sub>3</sub>OH and CH<sub>2</sub>DOH (Figure 9(c)). CH<sub>3</sub>OH and CH<sub>2</sub>DOH, having an extended distribution, show high temperatures even in the outer parts (Figures 9(b) and (c)). The different temperature distributions suggest that the outer region is heated by some mechanisms other than the radiation from the central source.

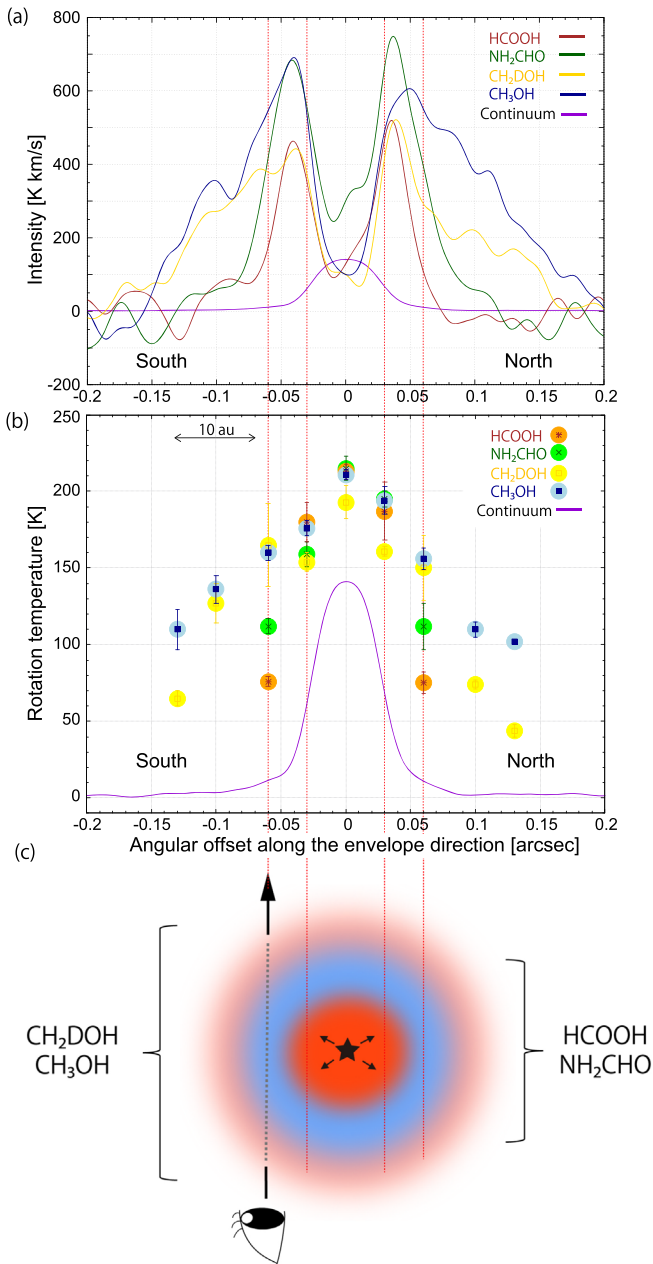


**Figure 9.** (a) Intensity profiles of the HCOOH ( $12_{0,12} - 11_{0,11}$ ), NH<sub>2</sub>CHO ( $12_{0,12} - 11_{0,11}$ ), CH<sub>2</sub>DOH ( $4_{2,2} - 4_{1,3}$ ,  $e_0$ ), CH<sub>3</sub>OH ( $4_{2,2} - 5_{1,5}$ , A) lines, and the dust continuum emission along the envelope direction (Figure 1). The intensity depression of the molecular lines at the continuum peak is due to the high dust opacity. (b) Rotation temperature distribution along the envelope direction. The quoted errors are the fitting error of the multiline analysis (Section 4.2). (c) Schematic illustration of the disk/envelope system. The temperature of the region in red is higher than that in blue. Accretion shock by an infalling gas raises the temperature of the outer part. The vertical red dotted lines just relate the three panels.

This situation can be explained by the temperature structure schematically shown in Figure 9(c). As the disk/envelope system of B335 is close to an edge-on configuration, the temperature derived in the above analysis is an effective one averaged over the line of sight. If the outer envelope is heated by some mechanisms rather than by the protostar radiation, the temperature derived for CH<sub>3</sub>OH and CH<sub>2</sub>DOH along the line of sight shown in Figure 9(c) can effectively be higher than that for HCOOH and NH<sub>2</sub>CHO due to the contribution of the outer envelope having a higher temperature.

### 4.3. An Implication of the Accretion Shock

What is the origin for the above temperature structure? An accretion shock can be a possible explanation for the difference in the rotation temperature at the positions of  $\pm 0''.06$ . In general, an infalling-rotating gas cannot fall beyond a certain radius, unless the angular momentum of the gas is extracted by some mechanism. This radius is called a centrifugal barrier and corresponds to half of the centrifugal radius (Sakai et al. 2014b; Oya et al. 2016). The gas is stagnated in front of the centrifugal barrier, and an accretion shock is formed by the infalling gas there (Sakai et al. 2017). In this case, the centrifugal barrier in B335 would roughly be estimated to be around the radius of  $\sim 0''.06$  ( $\sim 10$  au) from the continuum peak. This is almost consistent with the previous estimate of  $< 8$  au based on the gas kinematics (Imai et al. 2019). As the CH<sub>3</sub>OH and CH<sub>2</sub>DOH emission are weaker outside the radius of  $0''.1$  despite the large recoverable scale of  $0''.3$  (Figure 9(c)), a larger radius of the centrifugal barrier would be ruled out. According to the PV diagram of PC1, the gas is infalling and rotating, and the line-of-sight gas velocity at the radius of  $0''.06$  is about  $3 \text{ km s}^{-1}$  with respect to the systemic velocity ( $8.34 \text{ km s}^{-1}$ ; Yen et al. 2015). If this velocity can contribute to the shock, the temperature can be raised up to about 300 K for the adiabatic case (Duley & Williams 1984; Aota et al. 2015; Miura et al. 2017; Yamamoto 2017). Hence, accretion shock heating is indeed possible.

A similar idea is reported for the other protostellar source, IRAS 16293–2422 Source A, by Oya & Yamamoto (2020). They derived the rotation temperature of H<sub>2</sub>CS along the disk/envelope system of IRAS 16293–2422 Source A at a resolution of  $\sim 14$  au and found that the temperature profile within the radius of 50 au is flattened. This feature is most likely due to the local steep rise around 50 au. The derived profile cannot be explained by only the radiation heating by the central protostar (A1), and hence, they suggest the accretion shock as another heating mechanism.

If the inside and outside of the disk/envelope system are heated by the protostar radiation and the accreting gas, respectively, the radial temperature profile as a function of the distance from the protostar would have a local minimum between the inner and outer regions (Figure 9(c)). This situation results in the ring-like structure of an enhanced temperature region surrounding the disk/envelope system. This is also indicated by the model study reported in Fateeva et al. (2011).

In our observation, the ring-like structure is not observed because the disk/envelope system is almost edge-on (Figure 1(c)). However, the derived temperatures depend on the molecules at  $\pm 0''.06$ , where the compactly distributed HCOOH and NH<sub>2</sub>CHO lines show the relatively lower temperatures, suggesting the temperature decrease around the boundary between the inner and outer regions (Figure 9(b)). In contrast, the rotation temperature of CH<sub>3</sub>OH remains high there due to the contribution of the high temperature gas in the outer part along the line of sight. This picture is further supported by the fact that the CH<sub>3</sub>OH temperatures at the positions of  $\pm 0''.1$  in the north and the south are higher than 100 K despite a weak dust emission (Figure 9(b) and Table 5). Moreover, it should be noted that the equally high temperature of CH<sub>3</sub>OH at  $\pm 0''.06$  on both the north and south sides suggests that the temperature raise in the north would not be due to the possible outflow shock on the northwestern part where the CH<sub>3</sub>OH intensity enhancement is seen.

**Table 5**  
Rotation Temperature and Column Density along the Envelope Direction<sup>a</sup>

Temperature (K)									
Position	Offset (")	HCOOH		NH <sub>2</sub> CHO		CH <sub>2</sub> DOH		CH <sub>3</sub> OH	
1	0.13	...	...	...	...	44	(4)	102	(0.2)
2	0.10	...	...	...	...	74	(3)	110	(5)
3	0.06	75	(7)	112	(15)	150	(21)	156	(7)
4	0.03	187	(19)	195	(5)	161	(3)	194	(9)
Continuum peak	0	213	(5)	215	(8)	193	(11)	211	(3)
5	-0.03	180	(13)	159	(8)	154	(6)	176	(5)
6	-0.06	76	(3)	112	(5)	165	(27)	160	(5)
7	-0.10	...	...	...	...	127	(13)	136	(9)
8	-0.13	...	...	...	...	65	(5)	110	(13)

Column density (10 <sup>18</sup> cm <sup>-2</sup> )									
Position	Offset (")	HCOOH		NH <sub>2</sub> CHO		CH <sub>2</sub> DOH		CH <sub>3</sub> OH	
1	0.13	...	...	...	...	1.2	(0.9)	1.6	(0.01)
2	0.10	...	...	...	...	0.67	(0.15)	4.6	(1.0)
3	0.06	0.17	(0.09)	0.17	(0.07)	0.89	(0.07)	7.9	(2.5)
4	0.03	0.54	(0.21)	0.31	(0.03)	2.5	(0.1)	17	(9)
Continuum peak	0	1.1	(0.4)	0.18	(0.05)	2.5	(1.4)	8.5	(2.3)
5	-0.03	0.38	(0.07)	0.37	(0.09)	2.2	(0.3)	16	(7)
6	-0.06	0.22	(0.04)	0.17	(0.02)	1.1	(0.1)	8.6	(1.9)
7	-0.10	...	...	...	...	0.83	(0.15)	4.8	(1.6)
8	-0.13	...	...	...	...	0.49	(0.35)	2.4	(1.8)

**Note.**

<sup>a</sup> The rotation temperatures and the column densities derived from a multiline analysis (Section 4.1). Numbers in parentheses denote the fitting error in the least-square analysis. The envelope direction and the position numbers are shown in Figure 1(b).

Thus, our results suggest that the accretion shock heating occurs at the radius of 0''.06 or larger. It is worth noting that the HCOOH and NH<sub>2</sub>CHO lines are not seen in the outer region despite the temperature at which the ice mantles would be sublimated. Hence, HCOOH and NH<sub>2</sub>CHO may not simply be supplied from dust grains even in the inner envelope. This point is discussed in the next section.

### 5. HCOOH and Nitrogen-bearing Species

As mentioned in Section 1, the different distributions of nitrogen-bearing COMs and oxygen-bearing COMs have been revealed in star-forming regions. Furthermore, a specific distribution of HCOOH has also been pointed out. For instance, in the high-mass star-forming region, Orion KL, the distribution of HCOOH is reported to be different from other oxygen-bearing COMs such as HCOOCH<sub>3</sub> and (CH<sub>3</sub>)<sub>2</sub>O (Liu et al. 2002). Feng et al. (2015) revealed the similarity of the distribution of HCOOH to that of nitrogen-bearing COMs in Orion KL. Tercero et al. (2018) reported the differentiation among oxygen-bearing COMs within Orion KL, where the distribution of HCOOH is different from CH<sub>3</sub>OH. As such chemical differentiation is found in a complex structure of Orion KL on a scale of a few thousand au, the different distributions between nitrogen-bearing COMs and oxygen-bearing COMs as well as the specific distribution of HCOOH have been discussed in terms of the physical and chemical conditions and/or evolution history of subcomponents.

On the other hand, we have revealed the chemical differentiation within the disk/envelope system on a few au scale in B335. Our result of PCA-3D shows the compact distribution of nitrogen-bearing molecules. Moreover, the HCOOH lines are found to have a similar distribution to them.

Although such trends have recently been suggested for other low-mass protostellar sources: L483 (Oya et al. 2017; Okoda et al. 2021), S68N, and B1-c (Nazari et al. 2021), we have revealed the differentiation in relation to the temperature structure in B335. For the high-mass star-forming region G328.2551-0.5321, Csengeri et al. (2019) reported the compact distribution of HCOOH and the nitrogen-bearing COMs, which is essentially consistent with our result. We note that, in contrast, the distributions of CH<sub>3</sub>OH and HCOOH are reported to be similar to each other in the pre-stellar core L1544 (Jiménez-Serra et al. 2016).

HCOOH is the simplest carboxylic acid and has been observed toward high-mass and low-mass star-forming regions (e.g., Woods et al. 1983; Liu et al. 2001, 2002; Bisschop et al. 2007; Lefloch et al. 2017; Oya et al. 2017; Csengeri et al. 2019), protoplanetary disks (e.g., Favre et al. 2018), pre-stellar sources (e.g., Irvine et al. 1990; Vastel et al. 2014; Jiménez-Serra et al. 2016), and comets of the solar system (Biver et al. 2014). Although the production of HCOOH has also been investigated experimentally (Ioppolo et al. 2011) and theoretically (Tielens & Hagen 1982; Garrod & Herbst 2006; Aikawa et al. 2008; Garrod et al. 2008; Vasyunin et al. 2017), its formation process and chemical link to nitrogen-bearing species are puzzling. Indeed, the chemical network calculation tracing a pre-stellar/protostellar core by Aikawa et al. (2020) indicates that nitrogen-bearing COMs and HCOOH appear in the same region (i.e., a hot core) as oxygen-bearing COMs: no differentiation is found. It should be noted that the differentiation is not ascribed to the desorption temperature of these molecules formed on grain mantles. As described in Section 4.2, the temperature of the outer envelope traced by CH<sub>3</sub>OH is 150–165 K, which is higher than that of the inner

**Table 6**  
Fractional Abundances Relative to CH<sub>3</sub>OH around the Protostars

Source	B335 <sup>a</sup>	L483 <sup>b</sup>	B1-c <sup>c</sup>	S68N <sup>c</sup>	IRAS 16293 A <sup>d</sup>
[HCOOH]/[CH <sub>3</sub> OH]	0.02-0.03	...	$4.0 \times 10^{-4}$	$7.0 \times 10^{-4}$	$1.0 \times 10^{-3}$
[NH <sub>2</sub> CHO]/[CH <sub>3</sub> OH]	0.02	$5.9 \times 10^{-4}$	...	...	$1.5 \times 10^{-3}$
Resolution (au)	5	50	144	196	70

#### Notes.

<sup>a</sup> This work. These values are derived from the column densities at the offsets of  $\pm 0''.03$ , because the optical depth is high at the continuum peak.

<sup>b</sup> Jacobsen et al. (2019).

<sup>c</sup> B1-c in the Perseus Barnard 1 cloud and Serpens S68N (van Gelder et al. 2020).

<sup>d</sup> IRAS 16293-2422 Source A (Manigand et al. 2020).

envelope traced by HCOOH and NH<sub>2</sub>CHO, 75–112 K. Hence, ice mantles containing various COMs should have already been liberated from dust grains in the outer envelope. However, the results of PCA-3D suggest that HCOOH and the nitrogen-bearing species, NH<sub>2</sub>CHO, HNCO, and HC<sub>3</sub>N, do not appear in the gas phase outside the radius of  $\sim 0''.06$ , even though these desorption temperatures are comparable to those of CH<sub>3</sub>OH (e.g., Oya et al. 2019). In other words, other factors rather than the desorption temperature should be responsible for these molecules to be observed in the gas phase. It may be the high-density condition, protostellar radiation, or both of them. The gas-phase production of nitrogen-bearing COMs and HCOOH should be considered seriously.

In this relation, we briefly discuss the abundance ratios of HCOOH and NH<sub>2</sub>CHO relative to CH<sub>3</sub>OH. At offsets of  $\pm 0''.03$ , the HCOOH/CH<sub>3</sub>OH and NH<sub>2</sub>CHO/CH<sub>3</sub>OH ratios are 0.02–0.03. These values are higher than those found in other sources L483, B1-c, and S68N, and IRAS 16293-2422 Source A :  $10^{-3}$ – $10^{-4}$  (Jacobsen et al. 2019; Manigand et al. 2020; van Gelder et al. 2020), as shown in Table 6. Interestingly, we note that these ratios of B335 are comparable to those reported by the chemical network calculation (Garrod et al. 2022):  $10^{-2}$  for HCOOH/CH<sub>3</sub>OH and  $(1-6) \times 10^{-3}$  for NH<sub>2</sub>CHO/CH<sub>3</sub>OH. The NH<sub>2</sub>CHO/CH<sub>3</sub>OH ratio in IRAS 16293-2422 Source A is also consistent with the result of the chemical model. However, the other ratios shown in Table 6 are lower than the model results. There would be the two reasons for the discrepancy. First, the CH<sub>3</sub>OH abundance obtained in this study may be underestimated due to high optical depths of the observed lines. We consider the optical depth effect by using Equation (1), but it may not be sufficient. Second, the observed abundances of HCOOH and NH<sub>2</sub>CHO in the other sources may be underestimated due to the beam dilution effect, if their distribution is more compact than that of CH<sub>3</sub>OH, as found in this study. In fact, the resolution is relatively low for B1-c and S68N. For L483, the resolution of 50 au may not be enough to resolve the hot core (Table 6). In any case, we need more observations toward other protostars at a resolution of a few au scale to fully understand the chemical process of organic molecules. Related experimental and theoretical studies are also awaited.

## 6. Summary

We have conducted high-resolution observations of COMs in the low-mass Class 0 protostellar source B335 with ALMA. Our major findings are summarized below.

1. We perform PCA for the cube data of 32 molecular-line emission observed at a high angular resolution of  $0''.03$ . We

find that the distributions of the nitrogen-bearing molecules, NH<sub>2</sub>CHO, HNCO, and HC<sub>3</sub>N as well as HCOOH, are more compact than those of the oxygen-bearing species such as CH<sub>2</sub>DOH and CH<sub>3</sub>OH. Clear differentiations of COM distributions are thus identified on a few au scale around the protostar of B335.

2. We derive the rotation temperatures of the disk/envelope system under the assumption of LTE condition by using the multiline analysis of HCOOH, NH<sub>2</sub>CHO, CH<sub>2</sub>DOH, and CH<sub>3</sub>OH. Along the envelope direction, the temperatures at the radius of  $0''.06$  of CH<sub>3</sub>OH and CH<sub>2</sub>DOH (150–165 K) are found to be higher than those of HCOOH and NH<sub>2</sub>CHO (75–112 K). This result suggests that the outer envelope is heated by some mechanisms other than the protostellar radiation. We propose the accretion shock as the mechanism to account for, based on the temperature distribution.

3. The compact distributions of HCOOH and nitrogen-bearing molecules along with the temperature structure raise an important question on their formation mechanism. These molecules are not observed in the outer region where the temperature is higher than the sublimation temperature of the ice mantle ( $>100$  K). This result implies that they are not simply supplied from the ice mantle in the central part. Their production in the closest vicinity of the protostar should be considered.

We thank the reviewer for his/her invaluable comments and suggestions. This paper makes use of the following ALMA data set: ADS/JAO.ALMA# 2018.1.01311.S (PI: Muneaki Imai). ALMA is a partnership of the ESO (representing its member states), the NSF (USA) and NINS (Japan), together with the NRC (Canada) and the NSC and ASIAA (Taiwan), in cooperation with the Republic of Chile. The Joint ALMA Observatory is operated by the ESO, the AUI/NRAO, and the NAOJ. The authors thank the ALMA staff for their excellent support. This project is supported by a Grant-in-Aid from Japan Society for the Promotion of Science (KAKENHI: Nos. 18H05222, 19H05069, 19K14753, and 20J13783). Y. Okoda thanks the Advanced Leading Graduate Course for Photon Science (ALPS), Japan Society for the Promotion of Science (JSPS), and RIKEN Special Postdoctoral Researcher Program (Fellowships) for financial support.

## Appendix A PC3 and PC4 in PCA-3D

The distributions of PC3 and PC4 have the low signal-to-noise ratio in comparison with those of PC1 and PC2. The contribution ratios of PC3 and PC4 are 7.9% and 5.0%,

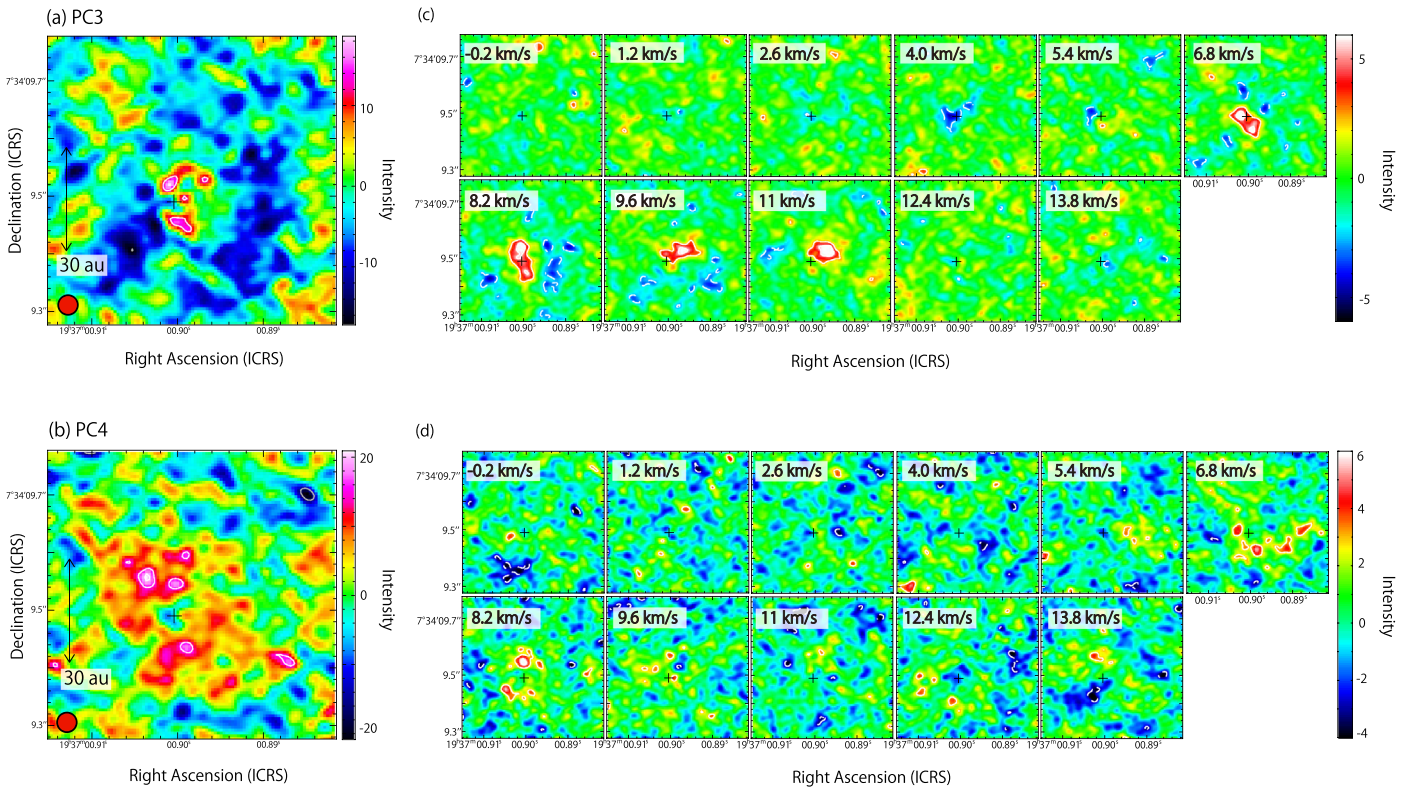


**Figure 10.** (a), (b) Moment 0 maps of the third and fourth principal components (PC3 and PC4) in PCA-3D. The velocity range of integration is from  $-0.2$  to  $14.5$   $\text{km s}^{-1}$ . Contour levels are every  $3\sigma$  from  $3\sigma$ , where  $\sigma$  is 5. The red circles show the beam size. (c), (d) Channel maps of the third and fourth principal components. Each panel represents the integrated intensity over a velocity range of  $1.4$   $\text{km s}^{-1}$  except for the last one (the panel of  $13.8$   $\text{km s}^{-1}$ ), whose lower-end velocity is quoted on the upper-left corner. The panel of  $13.8$   $\text{km s}^{-1}$  is integrated over a velocity range of  $0.7$   $\text{km s}^{-1}$ . The systemic velocity is  $8.34$   $\text{km s}^{-1}$ . Contour levels for PC3 (c) and PC4 (d) are every  $3\sigma$  from  $3\sigma$ , where  $\sigma$  is 0.9 and 1.0, respectively. The cross marks show the continuum peak position.

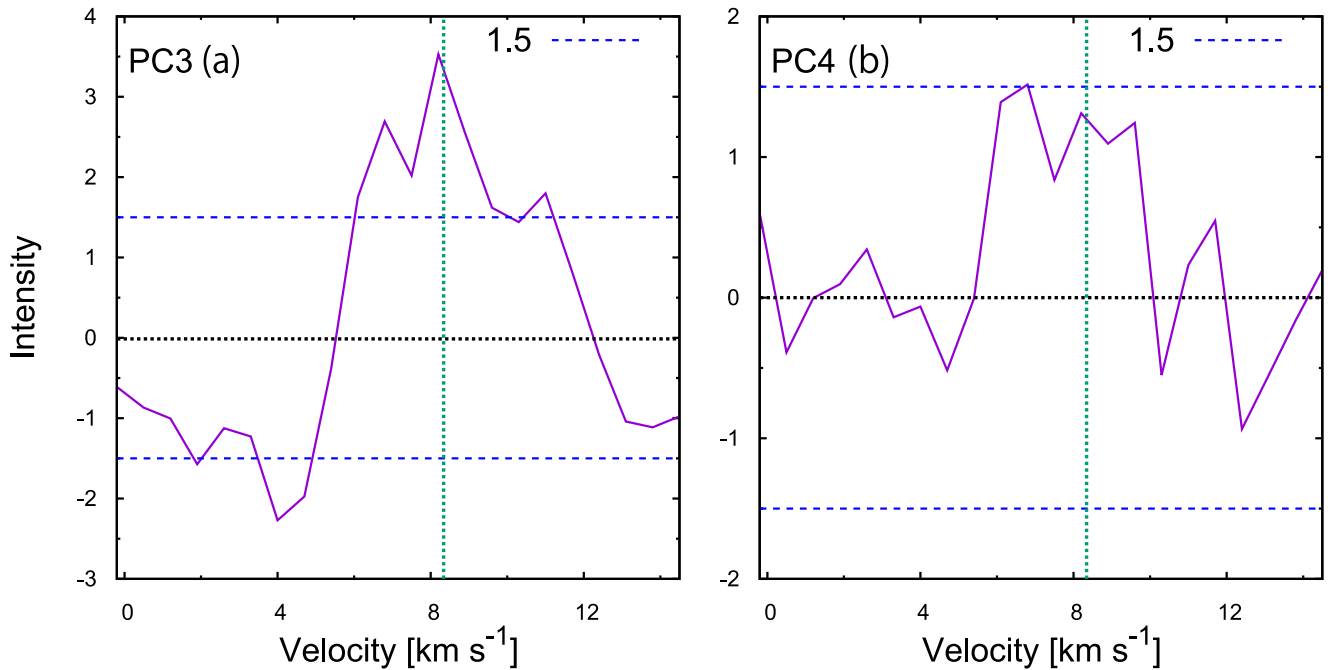
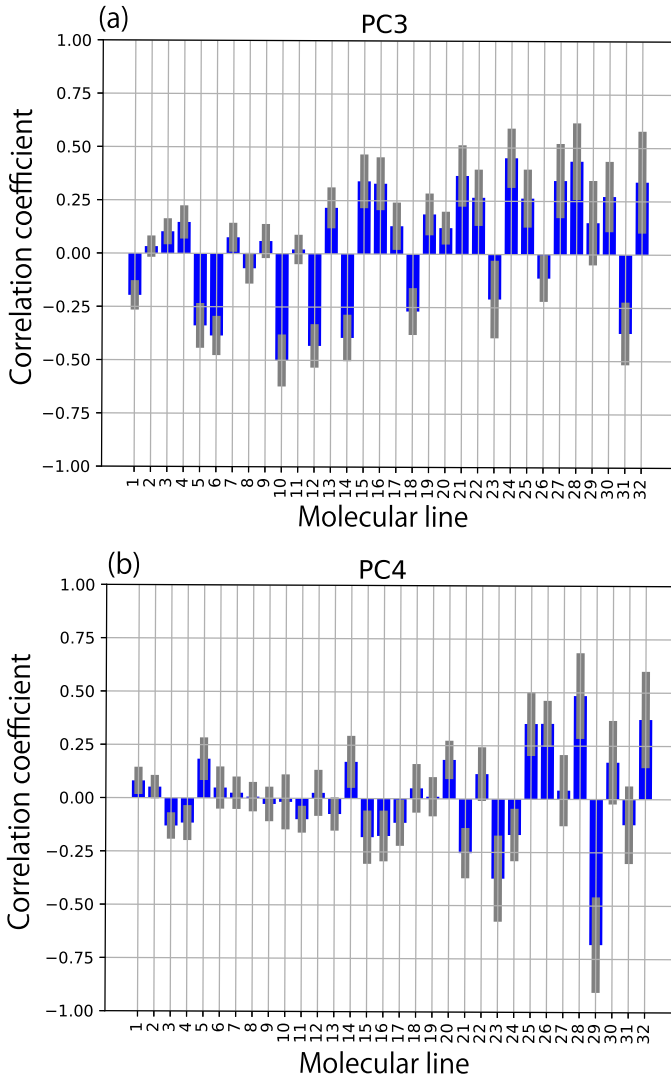


**Figure 11.** Spectral line profiles of the third and fourth principal components in PCA-3D. The spectra are prepared for a circular region with a diameter of  $0''.1$  centered at the continuum peak. The horizontal blue dashed lines represent  $\pm 3\sigma$  noise levels, where  $\sigma$  is 0.5. The horizontal black dotted lines represent the zero-level intensity. The vertical green dotted lines represent the systemic velocity of  $8.34$   $\text{km s}^{-1}$ .

respectively. Nevertheless, some structures are seen in each velocity channel map, as shown in Figure 10. We here describe the specific features of PC3 and PC4 and the

characteristics of the molecular lines extracted by them. The eigenvectors and eigenvalues for PC3 and PC4 are listed in Table 3.



1	CH <sub>3</sub> OH.18 <sub>3,15</sub> -18 <sub>2,16</sub> , A
2	CH <sub>3</sub> OH.21 <sub>3,18</sub> -21 <sub>2,19</sub> , A
3	CH <sub>3</sub> OH.12 <sub>6,7</sub> -13 <sub>5,8</sub> , E
4	CH <sub>3</sub> CHO.14 <sub>1,14</sub> -13 <sub>1,13</sub> , A
5	CH <sub>3</sub> OH.17 <sub>3,14</sub> -17 <sub>2,15</sub> , A
6	CH <sub>3</sub> OH.4 <sub>2,2</sub> -5 <sub>1,5</sub> , A
7	CH <sub>2</sub> DOH.4 <sub>2,2</sub> -4 <sub>1,3</sub> , e <sub>0</sub>
8	CH <sub>2</sub> DOH.5 <sub>2,4</sub> -5 <sub>1,5</sub> , e <sub>0</sub>
9	CH <sub>2</sub> DOH.3 <sub>2,1</sub> -3 <sub>1,2</sub> , e <sub>0</sub>
10	CH <sub>3</sub> OH.2 <sub>1,1</sub> -1 <sub>0,1</sub> , E
11	HNCO.12 <sub>0,12</sub> -11 <sub>0,11</sub>
12	CS.5-4
13	NH <sub>2</sub> CHO. 12 <sub>0,12</sub> -11 <sub>0,11</sub>
14	SO.7 <sub>6</sub> -6 <sub>5</sub>
15	CH <sub>2</sub> DOH.10 <sub>2,8</sub> -10 <sub>1,9</sub> , o <sub>1</sub>
16	H <sub>2</sub> CO.10 <sub>1,9</sub> -10 <sub>1,10</sub>
17	CHD <sub>2</sub> OH. J=6-5, K=1+, o <sub>1</sub>
18	HNCO.12 <sub>1,12</sub> -11 <sub>1,11</sub>
19	HCOOH.11 <sub>5,7</sub> -10 <sub>5,6</sub> and 11 <sub>5,6</sub> -10 <sub>5,5</sub>
20	SO <sub>2</sub> .10 <sub>3,7</sub> -10 <sub>2,8</sub>
21	HCOOH. 12 <sub>0,12</sub> -11 <sub>0,11</sub>
22	CHD <sub>2</sub> OH. J=6-5, K=1+, e <sub>0</sub>
23	CH <sub>3</sub> CHO.14 <sub>0,14</sub> -13 <sub>0,13</sub> , E, v <sub>t</sub> =1
24	HCOOH.11 <sub>6,6</sub> -10 <sub>6,5</sub> and 11 <sub>6,5</sub> -10 <sub>6,4</sub>
25	CH <sub>3</sub> OD.5 <sub>-1</sub> -4 <sub>0</sub> , E
26	HC <sub>3</sub> N.27-26
27	CH <sub>3</sub> OCHO.21 <sub>7,14</sub> -20 <sub>7,13</sub> , A
28	C <sub>2</sub> H <sub>5</sub> OH.13 <sub>2,12</sub> -12 <sub>1,11</sub>
29	CH <sub>3</sub> OCHO.21 <sub>7,14</sub> -20 <sub>7,13</sub> , E
30	CH <sub>3</sub> COCH <sub>3</sub> .14 <sub>11,3</sub> -13 <sub>10,4</sub>
31	CH <sub>2</sub> OHCHO.7 <sub>7,1</sub> -6 <sub>6,0</sub> and 7 <sub>7,0</sub> -6 <sub>6,1</sub>
32	CH <sub>3</sub> OCHO.20 <sub>11,10</sub> -19 <sub>11,9</sub> , E

**Figure 12.** (a), (b) Correlation coefficients between the principal components and the molecular lines. The uncertainties are shown in gray. The numbers represent the molecular lines listed in the attached table.

In Figure 10 (c), PC3 has a positive compact distribution with negative extended clumpy features from 6.8 to 11.0 km s<sup>-1</sup>. As shown in Figure 10(a), the intensity of the southern side is negatively brighter than that of the northern side. Meanwhile, PC4 shows a weak emission surrounding the continuum peak (Figure 10(b)), where the positive emissions can be seen particularly at the panels of 6.8 and 8.2 km s<sup>-1</sup> (Figure 10 (d)). In the spectral line profiles, PC3 has the

positive and negative peaks at redshifted and blueshifted velocities, respectively (Figure 11(a)). On the other hand, the intensity of PC4 toward the continuum peak shows a positive intensity near the systemic velocity (Figure 11(b)), although it is lower than 3 $\sigma$ . This is due to its extended and clumpy distribution.

Figure 12 shows the correlation coefficient between the molecular lines and the principal components. While all the

molecular lines have a correlation smaller than 0.5 for PC3, a few lines have a moderate correlation for PC3 (Figure 12(a)). For instance, the CS (#12) and CH<sub>3</sub>OH (2<sub>1,1</sub> – 1<sub>0,1</sub>, E) (#10) lines show negative correlation for PC3. Negative PC3 can represent a more extended distribution than PC1 in the southwestern part. Hence, it seems reasonable that the low-excitation line (2<sub>1,1</sub> – 1<sub>0,1</sub>, E) (#10) of CH<sub>3</sub>OH has a moderate contribution for PC3. On the other hand, PC4 has negative and positive correlations with CH<sub>3</sub>OCHO (#29) and C<sub>2</sub>H<sub>5</sub>OH (#28), respectively, in particular (Figure 12(b)). The moment 0 map of C<sub>2</sub>H<sub>5</sub>OH (#28) (Figures 3(a), (b)) is indeed similar to the moment 0 map of PC4.

Thus, PC3 and PC4 also contribute to the classification of the data and extract some features of the molecular lines, although their contribution ratios are small. 32 molecular-line

data are mostly reproduced by the first four components (PC1–PC4).

## Appendix B Calculation Results from the Multiline Analysis

We carry out the least-squares analysis on the observed intensities for each molecule at each position by using the method described in Section 4.1. Here, examples of the fitting results for the positions of  $\pm 0''.06$  are presented in Table 7. In this calculation, we consider the effect of the optical depth of the dust ( $\tau_{\text{dust}}$ ). The derived  $\tau_{\text{dust}}$  for each line are summarized in Table 8. The  $\tau_{\text{dust}}$  values derived from the analysis of different molecules at the continuum peak and the positions of  $\pm 0''.03$  differ by no more than 10%. Although those at positions of  $\pm 0''.06$  differ by 40% at most, the difference is not significant if the uncertainties ( $\sigma$ ) are taken into account.

**Table 7**  
Examples of the Multiline Analysis at the Offsets of  $\pm 0''.06$

Transition	Frequency (GHz)	$\Delta v$ (km s <sup>-1</sup> )	Intensity (K)	Residual <sup>b</sup> (K)	$\tau_{\text{line}}$	$\Delta v$ (km s <sup>-1</sup> )	Intensity (K)	Residual <sup>b</sup> (K)	$\tau_{\text{line}}$ <sup>c</sup>
HCOOH			$-0''.06^a$			$+0''.06^a$			
11 <sub>3,8</sub> – 10 <sub>3,7</sub>	248.2744893	4.9	54 (8)	–4.2	4.6	5.4	56 (12)	0.2	3.3
11 <sub>5,7</sub> – 10 <sub>5,6</sub> and 11 <sub>5,6</sub> – 10 <sub>5,5</sub>	247.5140000	7.1	57 (10)	1.9	2.8	6.1	63 (8)	9.7	2.5
11 <sub>6,6</sub> – 10 <sub>6,5</sub> and 11 <sub>6,5</sub> – 10 <sub>6,4</sub>	247.4462429	14	32 (8)	–0.4	0.8	5.4	40 (8)	–6.1	1.6
12 <sub>0,12</sub> – 11 <sub>0,11</sub>	262.1034810	5.2	61 (12)	2.6	6.7	3.5	54 (10)	–3.6	8.0
NH <sub>2</sub> CHO			$-0''.06$			$+0''.06$			
12 <sub>0,12</sub> – 11 <sub>0,11</sub>	247.3907190	4.9	97 (9)	2.8	17.5	3.5	87 (7)	–8.6	24.2
12 <sub>0,12</sub> – 11 <sub>0,11</sub> , $v_{12} = 1$	247.3273220	4.0	33 (8)	–3.6	0.5	5.4	42 (10)	12.4	0.4
13 <sub>0,13</sub> – 12 <sub>1,12</sub>	244.8542130	3.8	64 (12)	2.9	1.0	4.9	44 (13)	–8.8	0.8
CH <sub>2</sub> DOH			$-0''.06$			$+0''.06$			
3 <sub>2,1</sub> – 3 <sub>1,2</sub> , e <sub>0</sub>	247.6257463	4.2	97 (7)	–1.2	1.1	4.5	93 (13)	7.2	1.0
4 <sub>2,2</sub> – 4 <sub>2,3</sub> , e <sub>0</sub>	244.8411349	4.9	97 (13)	6.6	1.0	4.2	83 (15)	–6.5	1.1
5 <sub>2,4</sub> – 5 <sub>1,5</sub> , e <sub>0</sub>	261.6873662	4.0	128 (9)	4.2	1.8	3.8	115 (13)	1.4	1.9
10 <sub>2,8</sub> – 10 <sub>1,9</sub> , o <sub>1</sub>	244.9888456	4.0	71 (12)	–8.9	0.8	4.9	58 (8)	–1.9	0.6
CH <sub>3</sub> OH			$-0''.06$			$+0''.06$			
2 <sub>1,1</sub> – 1 <sub>0,1</sub> , E	261.805675	5.7	132 (15)	–10.2	6.3	4.5	151 (12)	12.7	7.9
4 <sub>2,2</sub> – 5 <sub>1,5</sub> , A	247.228587	5.2	139 (12)	–1.9	4.3	4.9	131 (13)	–6.2	4.5
12 <sub>6,7</sub> – 13 <sub>5,8</sub> , E	261.704409	4.5	110 (11)	–3.6	1.6	4.2	109 (9)	–1.5	1.6
17 <sub>3,14</sub> – 17 <sub>2,15</sub> , A	248.282424	5.9	140 (11)	–2.6	6.7	4.5	147 (14)	8.3	8.1
18 <sub>3,15</sub> – 18 <sub>2,16</sub> , A	247.610918	5.2	145 (6)	2.5	6.2	4.5	124 (6)	–14.5	6.6
21 <sub>3,18</sub> – 21 <sub>2,19</sub> , A	245.223019	4.9	148 (15)	10.7	3.2	4.2	142 (15)	7.9	3.4

### Notes.

<sup>a</sup> The distance from the continuum peak along the envelope (Figure 1).

<sup>b</sup> Residuals of the intensity in the least-square fit (obs.-calc.).

<sup>c</sup> Optical depth of the line. Numbers in the parentheses represent the rms noise of the spectrum at each position ( $\sigma$ ).

**Table 8**  
Dust Optical Depth ( $\tau_{\text{dust}}$ ) Derived in the Fit<sup>a</sup>

Position	Offset (")	HCOOH	NH <sub>2</sub> CHO	CH <sub>2</sub> DOH	CH <sub>3</sub> OH	$I_{\text{dust}}$ (K)
Continuum peak	0	1.15 <sup>+0.12</sup> <sub>-0.03</sub>	1.12 <sup>+0.13</sup> <sub>-0.01</sub>	1.41 <sup>+0.24</sup> <sub>-0.08</sub>	1.16 <sup>+0.10</sup> <sub>-0.04</sub>	141.1
1	0.13	...	...	0.07±0.07	0.03±0.03	2.4
2	0.10	...	...	0.03±0.04	0.02±0.03	1.9
3	0.06	0.17 <sup>+0.06</sup> <sub>-0.04</sub>	0.11 <sup>+0.04</sup> <sub>-0.02</sub>	0.08 <sup>+0.03</sup> <sub>-0.01</sub>	0.08±0.02	11.0
4	0.03	0.47 <sup>+0.09</sup> <sub>-0.03</sub>	0.45 <sup>+0.04</sup> <sub>-0.02</sub>	0.58 <sup>+0.06</sup> <sub>-0.03</sub>	0.45 <sup>+0.05</sup> <sub>-0.01</sub>	68.1
5	-0.03	0.44 <sup>+0.07</sup> <sub>-0.01</sub>	0.52 <sup>+0.07</sup> <sub>-0.01</sub>	0.54 <sup>+0.07</sup> <sub>-0.02</sub>	0.45 <sup>+0.05</sup> <sub>-0.02</sub>	61.7
6	-0.06	0.18 <sup>+0.06</sup> <sub>-0.05</sub>	0.11±0.03	0.07 <sup>+0.03</sup> <sub>-0.01</sub>	0.08±0.02	11.5
7	-0.10	...	...	0.03±0.02	0.03±0.02	3.4
8	-0.13	...	...	0.05±0.05	0.03±0.03	2.9

**Note.**

<sup>a</sup> The errors are estimated from the derived temperature based on the Equation (5).

**ORCID iDs**

Yuki Okoda  <https://orcid.org/0000-0003-3655-5270>  
 Yoko Oya  <https://orcid.org/0000-0002-0197-8751>  
 Muneaki Imai  <https://orcid.org/0000-0002-5342-6262>  
 Nami Sakai  <https://orcid.org/0000-0002-3297-4497>  
 Yoshimasa Watanabe  <https://orcid.org/0000-0002-9668-3592>  
 Ana López-Sepulcre  <https://orcid.org/0000-0002-6729-3640>  
 Kazuya Saigo  <https://orcid.org/0000-0003-1549-6435>  
 Satoshi Yamamoto  <https://orcid.org/0000-0002-9865-0970>

**References**

- Aikawa, Y., Furuya, K., Yamamoto, S., et al. 2020, *ApJ*, 897, 110  
 Aikawa, Y., Wakelam, V., Garrod, R. T., et al. 2008, *ApJ*, 674, 984  
 Ambrose, H. E., Shirley, Y. L., & Scibelli, S. 2021, *MNRAS*, 501, 347  
 Andre, P., Ward-Thompson, D., & Barsony, M. 2000, *Protostars and Planets IV* (Tucson, AZ: Univ. Arizona Press), 59  
 Aota, T., Inoue, T., & Aikawa, Y. 2015, *ApJ*, 799, 141  
 Arce, H. G., Santiago-García, J., Jørgensen, J. K., et al. 2008, *ApJL*, 681, L21  
 Bacmann, A., Taquet, V., Faure, A., et al. 2012, *A&A*, 541, L12  
 Beuther, H., Zhang, Q., Greenhill, L. J., et al. 2005, *ApJ*, 632, 355  
 Bianchi, E., Chandler, C. J., Ceccarelli, C., et al. 2020, *MNRAS*, 498, L87  
 Bisschop, S. E., Jørgensen, J. K., van Dishoeck, E. F., et al. 2007, *A&A*, 465, 913  
 Biver, N., Bockelée-Morvan, D., Debout, V., et al. 2014, *A&A*, 566, L5  
 Bjerkeli, P., Ramsey, J. P., Harsono, D., et al. 2019, *A&A*, 631, A64  
 Blake, G. A., Sutton, E. C., Masson, C. R., et al. 1987, *ApJ*, 315, 621  
 Bottinelli, S., Ceccarelli, C., Neri, R., et al. 2004, *ApJL*, 617, L69  
 Caselli, P., Hasegawa, T. I., & Herbst, E. 1993, *ApJ*, 408, 548  
 Charnley, S. B., Tielens, A. G. G. M., & Millar, T. J. 1992, *ApJL*, 399, L71  
 Calcutt, H., Jørgensen, J. K., Müller, H. S. P., et al. 2018, *A&A*, 616, A90  
 Caux, E., Kahane, C., Castets, A., et al. 2011, *A&A*, 532, A23  
 Cazaux, S., Tielens, A. G. G. M., Ceccarelli, C., et al. 2003, *ApJL*, 593, L51  
 Ceccarelli, C., Caselli, P., Fontani, F., et al. 2017, *ApJ*, 850, 176  
 Cernicharo, J., Marcelino, N., Roueff, E., et al. 2012, *ApJL*, 759, L43  
 Chahine, L., López-Sepulcre, A., Neri, R., et al. 2022, *A&A*, 657, A78  
 Codella, C., Ceccarelli, C., Bianchi, E., et al. 2020, *A&A*, 635, A17  
 Crockett, N. R., Bergin, E. A., Neill, J. L., et al. 2015, *ApJ*, 806, 239  
 Csengeri, T., Belloche, A., Bontemps, S., et al. 2019, *A&A*, 632, A57  
 De Simone, M., Codella, C., Ceccarelli, C., et al. 2020, *A&A*, 640, A75  
 Duan, Y.-B., Ozier, I., Tsunekawa, S., et al. 2003, *JMoSp*, 218, 95  
 Duley, W. W., & Williams, D. A. 1984, *Interstellar Chemistry* (London: Academic Press)  
 Endres, C. P., Schlemmer, S., Schilke, P., et al. 2016, *JMoSp*, 327, 95  
 Evans, N. J., Di Francesco, J., Lee, J.-E., et al. 2015, *ApJ*, 814, 22  
 Fateeva, A. M., Bisikalo, D. V., Kaygorodov, P. V., et al. 2011, *Ap&SS*, 335, 125  
 Favre, C., Fedele, D., Semenov, D., et al. 2018, *ApJL*, 862, L2  
 Feng, S., Beuther, H., Henning, T., et al. 2015, *A&A*, 581, A71  
 Fontani, F., Pascucci, I., Caselli, P., et al. 2007, *A&A*, 470, 639  
 Garrod, R. T., & Herbst, E. 2006, *A&A*, 457, 927  
 Garrod, R. T., Jin, M., Matis, K. A., et al. 2022, *ApJS*, 259, 1  
 Garrod, R. T., Wadsworth Weaver, S. L., & Herbst, E. 2008, *ApJ*, 682, 283  
 Herbst, E., & van Dishoeck, E. F. 2009, *ARA&A*, 47, 427  
 Hirano, N., Kameya, O., Kasuga, T., et al. 1992, *ApJL*, 390, L85  
 Hirano, N., Kameya, O., Nakayama, M., et al. 1988, *ApJL*, 327, L69  
 Imai, M., Oya, Y., Svoboda, B., et al. 2022, *ApJ*, 934, 70  
 Imai, M., Oya, Y., Sakai, N., et al. 2019, *ApJL*, 873, L21  
 Imai, M., Sakai, N., Oya, Y., et al. 2016, *ApJL*, 830, L37  
 Ioppolo, S., van Boheemen, Y., Cuppen, H. M., et al. 2011, *MNRAS*, 413, 2281  
 Irvine, W. M., Friberg, P., Kaifu, N., et al. 1990, *A&A*, 229, L9  
 Jacobsen, S. K., Jørgensen, J. K., Di Francesco, J., et al. 2019, *A&A*, 629, A29  
 Jiménez-Serra, I., Vasyunin, A. I., Caselli, P., et al. 2016, *ApJL*, 830, L6  
 Jiménez-Serra, I., Vasyunin, A. I., Spezzano, S., et al. 2021, *ApJ*, 917, 44  
 Jolliffe, I. T. 1986, *Principal Component Analysis* (New York: Springer)  
 Jørgensen, J. K., Müller, H. S. P., Calcutt, H., et al. 2018, *A&A*, 620, A170  
 Jørgensen, J. K., van der Wiel, M. H. D., Coutens, A., et al. 2016, *A&A*, 595, A117  
 Kang, M., Choi, M., Wyrowski, F., et al. 2021, *ApJS*, 255, 2  
 Keene, J., Hildebrand, R. H., Whitcomb, S. E., et al. 1980, *ApJL*, 240, L43  
 Kuan, Y.-J., Huang, H.-C., Charnley, S. B., et al. 2004, *ApJL*, 616, L27  
 Lee, C.-F., Codella, C., Li, Z.-Y., et al. 2019, *ApJ*, 876, 63  
 Lefloch, B., Ceccarelli, C., Codella, C., et al. 2017, *MNRAS*, 469, L73  
 Liu, S.-Y., Girart, J. M., Remijan, A., et al. 2002, *ApJ*, 576, 255  
 Liu, S.-Y., Mehringer, D. M., & Snyder, L. E. 2001, *ApJ*, 552, 654  
 Manigand, S., Jørgensen, J. K., Calcutt, H., et al. 2020, *A&A*, 635, A48  
 Martín-Doménech, R., Bergner, J. B., Öberg, K. I., et al. 2021, *ApJ*, 923, 155  
 McMullin, J. P., Waters, B., Schiebel, D., et al. 2007, in *ASP Conf. Ser. 376*, *Astronomical Data Analysis Software and Systems XVI* (San Francisco, CA: ASP), 127  
 Miura, H., Yamamoto, T., Nomura, H., et al. 2017, *ApJ*, 839, 47  
 Mukhopadhyay, I. 2016, *InPhT*, 75, 139  
 Nagy, Z., Spezzano, S., Caselli, P., et al. 2019, *A&A*, 630, A136  
 Nazari, P., van Gelder, M. L., van Dishoeck, E. F., et al. 2021, *A&A*, 650, A150  
 Ohashi, N., Hayashi, M., Ho, P. T. P., et al. 1997, *ApJ*, 475, 211  
 Okoda, Y., Oya, Y., Abe, S., et al. 2021, *ApJ*, 923, 168  
 Okoda, Y., Oya, Y., Sakai, N., et al. 2020, *ApJ*, 900, 40  
 Olofsson, S., & Olofsson, G. 2009, *A&A*, 498, 455  
 Oya, Y., López-Sepulcre, A., Sakai, N., et al. 2019, *ApJ*, 881, 112  
 Oya, Y., Moriwaki, K., Onishi, S., et al. 2018, *ApJ*, 854, 96  
 Oya, Y., Sakai, N., López-Sepulcre, A., et al. 2016, *ApJ*, 824, 88  
 Oya, Y., Sakai, N., Sakai, T., et al. 2014, *ApJ*, 795, 152  
 Oya, Y., Sakai, N., Watanabe, Y., et al. 2017, *ApJ*, 837, 174  
 Oya, Y., & Yamamoto, S. 2020, *ApJ*, 904, 185  
 Pickett, H. M., Poynter, R. L., Cohen, E. A., et al. 1998, *J. Quant. Spec. Radiat. Transf.*, 60, 883  
 Pineda, J. E., Maury, A. J., Fuller, G. A., et al. 2012, *A&A*, 544, L7  
 Sakai, N., Sakai, T., Hirota, T., et al. 2008, *ApJ*, 672, 371  
 Sakai, N., & Yamamoto, S. 2013, *ChRv*, 113, 8981  
 Sakai, N., Oya, Y., Higuchi, A. E., et al. 2017, *MNRAS*, 467, L76  
 Sakai, N., Oya, Y., Sakai, T., et al. 2014b, *ApJL*, 791, L38  
 Scibelli, S., Shirley, Y., Vasyunin, A., et al. 2021, *MNRAS*, 504, 5754  
 Scibelli, S., & Shirley, Y. 2020, *ApJ*, 891, 73  
 Soma, T., Sakai, N., Watanabe, Y., et al. 2018, *ApJ*, 854, 116  
 Spezzano, S., Caselli, P., Bizzocchi, L., et al. 2017, *A&A*, 606, A82

- Stutz, A. M., Rubin, M., Werner, M. W., et al. 2008, [ApJ](#), **687**, 389
- Sugimura, M., Yamaguchi, T., Sakai, T., et al. 2011, [PASJ](#), **63**, 459
- Taquet, V., Bianchi, E., Codella, C., et al. 2019, [A&A](#), **632**, A19
- Tercero, B., Cuadrado, S., López, A., et al. 2018, [A&A](#), **620**, L6
- Tielens, A. G. G. M., & Hagen, W. 1982, [A&A](#), **114**, 245
- Tychoniec, L., van Dishoeck, E. F., van't Hoff, M. L. R., et al. 2021, [A&A](#), **655**, A65
- van Gelder, M. L., Tabone, B., Tychoniec, L., et al. 2020, [A&A](#), **639**, A87
- van't Hoff, M. L. R., Harsono, D., Tobin, J. J., et al. 2020a, [ApJ](#), **901**, 166
- van't Hoff, M. L. R., van Dishoeck, E. F., Jørgensen, J. K., et al. 2020b, [A&A](#), **633**, A7
- Vastel, C., Ceccarelli, C., Lefloch, B., et al. 2014, [ApJL](#), **795**, L2
- Vasyunin, A. I., Caselli, P., Dulieu, F., et al. 2017, [ApJ](#), **842**, 33
- Watanabe, Y., Sakai, N., López-Sepulcre, A., et al. 2017, [ApJ](#), **847**, 108
- Watson, D. M. 2020, [RNAAS](#), **4**, 88
- Woods, R. C., Gudeman, C. S., Dickman, R. L., et al. 1983, [ApJ](#), **270**, 583
- Wright, M. C. H., Plambeck, R. L., & Wilner, D. J. 1996, [ApJ](#), **469**, 216
- Wyrowski, F., Schilke, P., Walmsley, C. M., et al. 1999, [ApJL](#), **514**, L43
- Yamamoto, S. 2017, Introduction to Astrochemistry: Chemical Evolution from Interstellar Clouds to Star and Planet Formation, Astronomy and Astrophysics Library (Japan: Springer), 2017
- Yen, H.-W., Takakuwa, S., Koch, P. M., et al. 2015, [ApJ](#), **812**, 129